Local calcium accumulations promote phagocyte-mediated synapse removal in cortical neuroinflammation

Mehrnoosh Jafari [1,2]†, Adrian-Minh Schumacher[1,2]†, Nicolas Snaidero[1,3,4]†, Emily M. Ullrich Gavilanes[1,2], Tradite Neziraj[1,2], Virág Kocsis-Jutka[1,2], Daniel Engels[1,2], Tanja Jürgens[5], Ingrid Wagner[5], Juan Daniel Flórez Weidinger[6,7,8,9], Stephanie S. Schmidt[1], Eduardo Beltrán[1,2], Nellwyn Hagan[10], Lisa Woodworth[10], Dimitry Ofengeim[10], Joseph Gans[11], Fred Wolf[6,7,8,9], Mario Kreutzfeldt[5,12], Ruben Portugues[13,14], Doron Merkler[5,12]*#, Thomas Misgeld[3,4,14]*# and Martin Kerschensteiner[1,2,14]*#

[1] Institute of Clinical Neuroimmunology, University Hospital, Ludwig-Maximilians Universität München, Munich, Germany

[2] Biomedical Center (BMC), Faculty of Medicine, Ludwig-Maximilians Universität München, Martinsried, Germany

[3] Institute of Neuronal Cell Biology, Technische Universität München, Munich, Germany

[4] German Center for Neurodegenerative Diseases (DZNE), Munich, Germany

[5] Department of Pathology and Immunology, University of Geneva, Geneva, Switzerland

[6] Theoretical Neurophysics, Max Planck Institute for Dynamics and Self-Organization, Göttingen, Germany

[7] Bernstein Center for Computational Neuroscience, University of Göttingen, Göttingen, Germany

[8] Max Planck Institute for Experimental Medicine, Göttingen, Germany.

[9] Center for Biostructural Imaging of Neurodegeneration, Göttingen, Germany.

[10] Sanofi Neuroscience, Framingham, MA, USA

[11] Translational Sciences Genomics, Sanofi, Framingham, MA, USA

[12] Division of Clinical Pathology, Geneva University Hospital, Geneva, Switzerland

[13] Sensorimotor Control, Max Planck Institute of Neurobiology, Martinsried, Germany

[14] Munich Cluster for Systems Neurology (SyNergy), Munich, Germany

† These authors contributed equally to this work.

Co-senior authors

*Correspondence to:
M.K. (martin.kerschensteiner@med.uni-muenchen.de)
D.M. (doron.merkler@unige.ch)
T.M. (thomas.misgeld@tum.de)

Words: 4,257 *Figures:* 6 (+ 12 Suppl. Figures) *Multimedia:* 1 Movie *References:* 77

ABSTRACT

Cortical pathology contributes to chronic cognitive impairment of patients suffering from the neuroinflammatory disease multiple sclerosis (MS). How such gray matter inflammation affects neuronal structure and function is not well understood. Here we use functional and structural *in vivo* imaging in a mouse model of cortical MS to demonstrate that bouts of cortical inflammation disrupt cortical circuit activity coincident with a widespread, but transient loss of dendritic spines. Spines destined for removal show local calcium accumulations and are subsequently removed by invading macrophages or activated microglia. Targeting phagocyte activation with a new antagonist of the colony-stimulating factor 1 receptor prevents cortical synapse loss. Overall, our study identifies synapse loss as a key pathological feature of inflammatory gray matter lesions that is amenable to immunomodulatory therapy.

KEYWORDS: Multiple sclerosis, neuroinflammation, gray matter pathology, microglia, macrophages, synapse loss, calcium imaging, *in vivo* imaging, two-photon microscopy, neuroprotection

INTRODUCTION

Multiple sclerosis (MS) is a common and severe inflammatory disease of the central nervous system (CNS), clinically characterized by distinct phases. In most cases MS is initially dominated by bouts of acute neuroinflammation that result in formation of focal white matter lesions and can be targeted therapeutically [1]. In contrast, the later progressive phase of the disease remains largely refractory to current therapeutic interventions and clinically appears reminiscent of classical neurodegenerative conditions. Indeed, it is increasingly recognized that pathology in the gray matter including the cortex is central to the progression of MS [2]. Gray matter pathology correlates with accruing disability, predicts conversion to progressive MS and explains the increasing cognitive deficits that MS patients with advanced disease experience [3-5]. Despite this profound clinical importance, our understanding of the mechanisms underlying cortical pathology in progressive MS remains poor, in part because modelling gray matter inflammation has been difficult. Moreover, the neuroimaging and neuropathology approaches used thus far provide insufficient spatial and temporal resolution to unravel the neurodegenerative mechanisms resulting from cortical inflammation.

Gray matter pathology in progressive MS is characterized by inflammation dominated by innate immune cells, extensive loss of cortical myelin and some neuronal cell death [2,6,7]. Of note, synapse loss might be a key neuronal pathology in such gray matter lesions as it occurs widespread throughout both the demyelinated, as well as the non-demyelinated, i.e. “normal-appearing” gray matter [8,9]. Thus, in cortical MS, just as in classical neurodegenerative diseases, the synapse might be the initiation site of neuronal damage. However, thus far it remains largely unknown, whether such synapse loss in cortical MS has a local functional correlate, how it is mediated, whether it is reversible, and if or how it could be prevented by appropriate therapeutic intervention.

In vivo imaging of the mouse cortex allows assessing local circuit function [10], the corresponding structural correlates [11] as well as the cellular mechanisms of neurodegeneration [12,13]. With the recent development of rodent models of cortical neuroinflammation by others and us [7,14–16], imaging of MS-related pathology in cortical circuits has become possible. Here we interrogated the structural and functional neuronal consequences of such inflammatory changes using a range of *in vivo* imaging modalities. We show that widespread synapse loss is induced in the inflamed mouse cortex, which mimics cortical MS lesions and surrounding gray matter. This synapse loss was present across cortical layers, preferentially affected excitatory inputs and was accompanied by diminished neuronal activity. Once cortical inflammation receded, synaptic connectivity recovered and cortical neurons re-established their original firing patterns. Notably, in active inflammatory lesions, spines characterized by local calcium overload were preferentially removed – with the removal process being mediated by activated microglia, as well as infiltrating macrophages. Finally, blunting the activation, invasion and phagocytic activity of these immune cells by blocking signaling through the colony-stimulating factor 1 receptor (CSF1-R) protected synapses from removal, suggesting that phagocyte-mediated synapse pruning might be a target to prevent progression of cortical MS pathology.

RESULTS

Widespread synapse loss is induced in a mouse model of cortical MS

To induce neuroinflammation in the mouse cortex, we adapted a targeted model of cortical MS pathology previously developed in rats [14,15]. We stereotactically injected interferon gamma (IFNγ) and tumor necrosis factor alpha (TNFα), pro-inflammatory cytokines highly expressed in the meninges of progressive MS patients [15,17], into the somatosensory cortex of mice that were previously immunized with myelin-oligodendrocyte glycoprotein (MOG, **Figure 1a**). This resulted in the formation of cortical lesions that extended subpially to both hemispheres (**Figure 1b**) thus mimicking the widespread cortical pathology in progressive MS. Like their counterparts in human MS [7,18], these cortical lesions were

characterized by phagocyte activation and modest T cell infiltration causing extensive myelin loss with relative preservation of axons (**Supplementary Figure 1**). To explore, whether such experimental gray matter lesions also reproduce the pervasive synaptic pathology observed in MS cortex [8], we reconstructed the dendrites of sparsely labeled layer III and layer V cortical projection neurons in *Thy1-GFP-M x BiozziABH* mice (**Figure 1c-1e**). We found that the density of dendritic spines was significantly reduced in both layers (**Figure 1f** and **1g**) at the acute stage of the cortical MS (c-MS) model (3 days post cytokine injection, d3 pci). Spine loss was observed ipsi- and contralaterally to the cytokine injection and was absent in mice that received either MOG immunization or cytokine injection alone (**Supplementary Figure 2**). Notably, spine loss was reversible, and spine density spontaneously recovered (**Figure 1h**). Electron microscopy (EM) confirmed the transient reduction of cortical synapse density (**Figure 1i** and **1j**), indicating that synapse loss is not restricted to cortical projection neurons, but rather a global feature of the inflamed cortex. While synapse loss thus seemed to be present in different neuronal cell populations, it did not appear to affect all synapses equally, as quantitative immunofluorescence analysis revealed a preferential loss of excitatory synapses, while the density of inhibitory synapses remained largely unchanged (**Figure 1k-1n**). This differential synapse loss resulted in a marked shift of the ratio between excitatory and inhibitory inputs and suggests that inhibition might dominate in the inflamed cortex (**Figure 1o**).

Cortical inflammation results in reversible neuronal silencing

A transient predominance of inhibition predicts a parallel reduction in cortical activity. To test this prediction, we performed chronic calcium imaging in the somatosensory cortices of lightly anaesthetized mice using recombinant adeno-associated virus (rAAV)-expressed GCaMP6s. We recorded spontaneous calcium activity in populations of individual layer II/III neurons from before cortical lesion induction (4 days before cytokine injection), to the peak of synapse loss (d3 pci) and finally to the synapse recovery phase (d10 and 17 pci; **Figure 2a** and **Supplementary Movie 1**). We observed a shift towards lower

frequencies of calcium transients with a significant drop in mean activity in acute gray matter lesions (**Figure 2b** and **2c**) consistent with neuronal silencing as a consequence of lost excitatory synaptic input [10]. In parallel, we observed a concomitant silencing and spine density reduction of the apical dendrites of layer V projection neurons that we recorded and reconstructed in *Thy1-GCaMP6f x BiozziABH* activity reporter mice [19] in the presence of cortical inflammation (**Supplementary Figure 3**).

Neuronal activity levels subsequently recovered in parallel with the restoration of synaptic connectivity (**Figure 2b** and **2c**). Activity changes are specific for the c-MS model, as no such alterations were observed in mice that received sham or cytokine injections only (**Figure 2c** and **Supplementary Figure 4**). Notably, in contrast to activity and synapse loss, which recovered within two weeks, myelin loss only partially reverted over this time period as evaluated by spectral confocal reflectance microscopy (SCoRe) imaging [20] and ultrastructural analysis (**Supplementary Figure 5**). Tracking activity levels of individual neurons over time further indicated that neurons that were more active before lesion induction typically resumed a similarly high activity level after recovery (**Figure 2d**). Moreover, when we compared the activity of individual neurons at d17 after the induction of cortical inflammation to their pre-lesion activity pattern, we found that these levels were as similar to each other as for neurons measured over the same time interval in sham injected mice (**Figure 3a**). This suggests that the inputs that determine the level of activity are either resilient or can be restored. To assess, whether only the average frequency of firing was robust across a bout of neuroinflammation (e.g. due to some intrinsic property of the individual neurons or homeostatic plasticity), or whether such robustness also extended to firing patterns across individual cells (e.g. due to re-emergence of the pre-lesion micro-circuitry), we analyzed the structure of pairwise correlations of individual neuronal activity patterns over different imaging sessions before, during and after cortical neuroinflammation (**Figure 3b-3d**). Our results show that the session-to-initial-session similarity (r_{signal}) drops significantly during acute cortical inflammation (at d3 pci) compared to sham-injected mice, but during the resolution phase (at d10 and 17 pci; **Figure**

3e) approaches control levels of correlation. This indicates a remarkable robustness of neuronal circuits - either due to resilience or precise restoration of critical inputs – when confronted with transient inflammatory disruption [10].

Persistent local calcium accumulations predict spine loss

Given its functional significance, we explored how synapse loss is induced in the inflamed gray matter and how such damage remains restricted to a subset of spines, while leaving the dendrite and many neighboring spines intact. Disturbances in calcium homeostasis have been shown to signal incipient loss of axons or dendrites [12,21,22]. Therefore, we explored whether local calcium dysregulation was apparent at dendritic spines in inflamed cortex using rAAV-mediated expression of the ratiometric calcium sensor Twitch-2b [23] in a subset of cortical neurons. *In vivo* multiphoton imaging allowed us to record spine calcium levels in the apical dendritic tufts at a time when substantial synapse loss (d3 pci) was apparent in the c-MS model (**Figure 4a** and **4b**). About 6 % of spines in the inflamed cortical tufts indeed displayed a localized calcium overload (> mean + 3 SD of control spines; **Figure 4c** and **4d**), while calcium levels in neuronal somata and the vast majority of dendrites remained unchanged (**Supplementary Figure 6**). Notably, fast imaging of spine calcium dynamics revealed that high calcium spines showed a continuous elevation of basic calcium levels on top of which similar fluctuations were superimposed in both high and low calcium spines (**Figure 4e**). These observations are consistent with a persistent local accumulation of calcium that occurs independently of altered synaptic activity.

To better understand the relation between local calcium accumulations and spine loss, we tracked the fate of spines over time (**Figure 4 f-h**). Our results showed that the probability for spine removal rose with increasing calcium concentrations in the spines. When we then further separated the „high risk“ spines (with calcium levels > mean + 3 SD of the control population) in two groups, based on whether the calcium accumulation was limited to the spine or extended to the adjacent dendritic shaft, we

observed that dendritic calcium overload coincided with a major increase in the spine removal rate (**Figure g**).

In parallel to high calcium spine removal, several previously unaffected spines showed a rise in calcium during our observation time, creating a stable steady-state fraction of calcium high spines (**Figure 4f** and **4h**). This suggests a local and dynamic process of postsynaptic calcium overload that leads to the loss of ~1 % of cortical spines per hour. Within one day, this rate can nearly account for the total spine loss observed in the c-MS model (~30 %; **Figure 1** and **Figure 4b**), matching the transient nature of the acute inflammatory environment.

To study whether the local rise in calcium was indeed an important driver of spine removal, we buffered extracellular calcium by local EGTA application [22] to cortical MS lesions in vivo and measured the resulting calcium dynamics and spine turn-over. Extracellular calcium buffering reduced the appearance rate of new high calcium spines, improved the probability of pre-existing high calcium spines to re-establish calcium homeostasis and significantly decreased the rate of spine loss (**Figure 4i**). Taken together, these results indicate that local calcium accumulations destabilize spines in the inflamed gray matter and promote their subsequent removal.

Microglia and monocyte-derived macrophages execute synapse removal

We next assessed, which cells execute synapse removal in inflamed cortex. Mononuclear phagocytes are candidates, as the local activation of microglial and the infiltration of monocyte-derived macrophages coincides with synapse loss in the c-MS model (**Supplementary Figure 7**). To evaluate the contribution of these cells to synapse loss, we quantified synapse phagocytosis by confocal 3D reconstruction of brain tissue from mice with genetically labeled phagocytes (microglia, $CX_3CR\text{-}1^{GFP}$; invading macrophages, $Ccr2^{RFP}$) [24] stained for presynaptic (Synapsin-1), postsynaptic (PSD95 and Homer-1) and lysosomal (LAMP1) markers (**Figure 5a** and **5b**) and confirmed synapse uptake by EM (**Figure 5d**). Quantitative

analysis showed a marked increase in engulfed pre- and postsynaptic material (both within and outside the lysosomal compartment) in microglial cells in the c-MS model compared to control gray matter (**Figure 5c** and **5f**). Furthermore, monocyte-derived macrophages contained similar amounts of pre- and postsynaptic material as microglial cells (**Figure 5e** and **5g**). Taken together these results indicate that local microglial cells and infiltrating monocyte-derived macrophages collaboratively execute synapse removal in inflamed gray matter.

Targeted interference with CSF1 signaling prevents synapse loss in the c-MS model

Finally, we explored whether phagocyte-mediated synapse removal could be targeted therapeutically using a newly developed inhibitor of CSF1 signaling[25]. While such inhibitors lead to the depletion of microglial cells at high concentration [26], at lower concentration, as used here, they inhibit phagocyte activation and limit synapse loss in neurodegenerative disease models [25,27]. Indeed, systemic application of the CSF1-R inhibitor during cortical lesion formation rescued synapse pathology in the c-MS model (**Figure 6a-c**). This therapeutic effect appeared to be primarily mediated by an altered innate immune response, as no apparent effects on T cell infiltration in the cortical gray matter were observed (**Supplementary Figure 8**). To further interrogate the effects of CSF1-R inhibition on phagocyte responses, we FACS-sorted the following phagocyte populations from the inflamed CNS of *Ccr2$^{RFP/wt}$ x BiozziABH* mice treated with either the CSF1-R inhibitor or vehicle solution (**Figure 6d** and **6e**): CD45^{int}/CD11b^{int} cells, which correspond to resting microglial cells, as well as CD45^{high}/CD11b^{high} activated phagocytes. The latter we further differentiated in two subpopulations based on RFP expression, namely Ccr2^{RFP}-positive (Ccr2^{pos}) cells, which likely represent recently infiltrated (monocyte-derived) phagocytes vs. Ccr2^{RFP}-negative (Ccr2^{neg}) cells, presumed to be locally activated phagocytes [24]. FACS analysis of these populations showed that CSF1-R inhibition led to a selective reduction of the proportion of CD45^{high}/CD11b^{high}/Ccr2^{pos} phagocytes isolated from the inflamed CNS, while the expression of activation markers was selectively reduced in the CD45^{high}/CD11b^{high}/Ccr2^{neg}

phagocytes. No obvious differences were observed in either the proportion or activation stage of resting microglial cells (**Supplementary Figure 9**). RNAseq analysis of these cell populations further established that a marked change of the transcriptional profile in response to CSF1-R inhibition was only apparent in $CD45^{high}/CD11b^{high}/Ccr2^{neg}$ phagocytes, while only few differentially regulated genes were detected in resting microglial cells ($CD45^{int}/CD11b^{int}$) or $CD45^{high}/CD11b^{high}/Ccr2^{pos}$ phagocytes (**Figure 6f-h)**. Further analysis of the genes most-strongly regulated by CSF1-R signaling in these locally activated phagocytes revealed that CSF1-R inhibition likely involves two collaborating mechanisms: First, a reduced expression of CCL2 (**Supplementary Figure 9**), the major chemokine responsible for the infiltration of monocytes to the CNS [28]. Indeed, a reduced number of monocyte-derived phagocytes was detected by histopathological analysis of cortical lesions derived from mice treated with the CSF1-R inhibitor, while numbers of microglial cells remained equal (**Figure 6k, l** and **Supplementary Figure 10**), in line with the results of the FACS analysis (**Supplementary Figure 9**). Second, CSF1-R inhibition selectively altered the phenotype of the $CD45^{high}/CD11b^{high}/Ccr2^{neg}$ phagocyte population, as it diminishes APOE expression in these cells and thereby at least partially reverses the APOE-dependent disease-associated gene signature of these cells [29] towards a more homeostatic phenotype (**Figure 6i, j**). In line with such an altered phenotype, we also observed a reduced expression of scavenger receptors, such as the macrophage scavenger receptor 1 (MSR1) and the macrophage mannose receptor 1 (MRC1), as well as of genes such as CD68 and arginase-associated intracellular degradation pathways. To test whether this altered phagocyte phenotype would directly affect the capacity of local (but not infiltrating) phagocytes to remove synapses, we analyzed the lysosomal content and synapse uptake in *$CX_3CR\text{-}1^{GFP/wt}$ x BiozziABH* mice and *$Ccr2^{RFP/wt}$ x BiozziABH* mice after CSF1-R inhibition. In line with the transcriptomic analysis, we found a selective reduction of lysosomal content and uptake of presynaptic material in $CX_3CR\text{-}1^{GFP}$ expressing phagocytes that was not observed in the $Ccr2^{pos}$ cell population (**Figure 6m, 6n** and **Supplementary Figure 10**). In line with a direct effect of CSF1-R inhibition on synapse uptake, we further observed that exposure of cultured microglia cells to CSF1 increased their

uptake of synaptoneurosomes, an effect that was blocked by the CSF1-R inhibitor (**Supplementary Figure 9**).

Taken together our analyses indicate that the primary cell population responding to the CSF1-R inhibition are $CD45^{high}/CD11b^{high}/Ccr2^{neg}$ phagocytes. These mediate the therapeutic effect by reversing their disease-associated phenotype and ability to engulf synapses as well as dampening the recruitment of monocyte-derived macrophages (which are altered in number, but not in phenotype or synapse removal capacity). This dual mechanism of action thus controls both the central and the peripheral arm of the phagocyte response, which reduces inflammatory damage to synapses (**Figure 6o** and **6p**), and thereby effectively limits synapse loss in the inflamed cortex.

DISCUSSION

While MS in its classical manifestation is dominated by white matter pathology and resulting sensory-motor deficits, cortical symptoms, such as fatigue and subtle cognitive decline, also contribute to the patients' loss of quality of life as the disease progresses [2,30]. The structural correlate of these symptoms is widespread gray matter pathology, with profound synapse loss, both in areas of gray matter demyelination [31,32] and beyond [8,9]. Indeed, the degree of synapse loss in the MS cortex is comparable to that seen in early stages of classical neurodegenerative disorders, such as Alzheimer's disease [33]. While much has been learned from applying *in vivo* imaging to disease models of such neurodegenerative conditions, both at the structural [12,13] and the functional levels [34], our understanding of inflammatory gray matter pathology remains in its infancy. Thus, even very fundamental questions, such as whether structural and functional synapse changes are reversible, or which inflammatory mechanisms drive synapse loss remain largely unanswered. The recent ability to model MS-related cortical neuroinflammation, using cortically targeted EAE models, now allowed us to address these questions. Indeed, our murine c-MS model recapitulates the widespread and pronounced cortical synapse loss also

seen in MS [8,9]. Importantly, this model also enables measuring the activity of local cortical circuitry by calcium imaging. Here, we observed transient hypoactivity of cortical projection neurons (both in layer II/III and layer V) that tracks a preferential loss of excitatory inputs in the cortex. In contrast, in other settings of synapse loss, such as early amyloid pathology in a model of Alzheimer's disease, hyperactivity has been described [34], which in part might be explained by substantial changes in overall cellular geometry due to dendrite remodeling [35], which we found to be absent in cortical neuroinflammation. Furthermore, it is noteworthy, that in other models of Alzheimer's disease-related pathology, which e.g. also incorporate tau aggregation, hypoactivity is also predominant [36]. In any case, prevailing evidence of functional imaging in human MS points to altered activity and circuit disconnection [37], relating to the findings at the cellular level in our model.

Given the profound structural and functional pathology that emerges from a single bout of cortical neuroinflammation, a remarkable observation of our study is the fact that such deficits appear to be largely reversible once inflammation subsides. In this process synapse densities are restored to pre-lesion levels and neuronal activity hierarchies or correlations resume the stability trajectories of control mice. This suggests a substantial endogenous neuronal repair potential in cortex, where – in contrast to white matter – also advanced structural alterations can be reversed. Indeed, once an axon has been transected in an inflammatory white matter lesion, no regeneration is possible, and compensatory remodeling is the prevailing, but limited mode of recovery [38]. In contrast, we now observe in the c-MS model that synapse loss, which includes removal of both pre- and postsynaptic material, is reversible without lasting structural imprint. Indeed, even the correlation landscape of local networks – likely indicative of regional interconnectivity or synchronized inputs – re-approached control levels, similar to what has been observed during reestablishment of visual cortex connectivity after sensory deprivation, albeit in this case rather than spontaneous patterns, a specific functional feature of cortical sensory function (ocular dominance) was examined [10]. Importantly, this degree of reversibility contrasts with the sustained

damage apparent in human gray matter MS lesions. Beyond the obvious species difference, the two pathological processes differ in key respects – most importantly timing and local chronicity of an inflammatory environment. While the c-MS model involves only one episode of locally triggered neuroinflammation, driven by a single injection of cytokines, in MS sustained sources of such proinflammatory signaling exist, e.g. originating from lymphoid aggregates in the meninges, which correlate with increased levels of proinflammatory cytokines in the cerebrospinal fluid of corresponding patients [15,17]. However, such cytokines might well have complex effects, as for example TNFα can potentiate existing synaptic connections, and hence contribute to transient hyperactivity of cortical circuits, e.g. during the recovery phase of subcortical neuroinflammation [39]. Thus, other confounders, such as age or threshold effects of accumulating subtle damage that exhaust repair or compensation capacities might contribute to the lasting cortical deficits observed in progressive MS. Altogether, this argues that early intervention to prevent smoldering cortical inflammation from taking hold might allow endogenous recovery mechanisms to prevail and thereby counteract MS progression.

So what drives synapse removal and hence circuit dysfunction in cortical neuroinflammation? We find that phagocytes, including tissue-resident microglia and infiltrating ($Ccr2^{pos}$) macrophages engulf synaptic material. Such phagocyte-mediated synapse engulfment is also a hallmark of other neurodegenerative, neuroinfectious and neuropsychiatric disorders [27,40–42], which stresses the unity of destructive mechanisms shared across a broad range of cortical pathologies.

However, while some aspects of the way activated immune cells damage the CNS might be rather conserved, it should be kept in mind that the behavior of immune cells such as microglia within the CNS can be variable (e.g. as it is influenced by the underlying disease mechanism, but also by other variables such as sex [43]). Indeed, for phagocyte-mediated synapse removal, various mechanisms have been proposed and likely operate in parallel. For instance, in a model of viral encephalitis, virally infected

neurons express chemokines, such as CCL2 as 'attack-me signals', to attract the phagocytes that strip the neuron of its synapses [42]. Moreover, in development and neurodegeneration, dysfunctional synapses are tagged by components of the complement system, which phagocytes recognize as 'eat-me signals' to initiate engulfment [44]. To these executive mechanisms of phagocyte-mediated synapse stripping, we now add localized calcium dyshomeostasis as an early predictor of which synapses are fated for removal. Such calcium accumulations - which could have a range of causes, including presynaptic hyperactivity of individual or clustered inputs, but also altered postsynaptic clearance or amplification from intracellular stores - appear to be particularly predictive of removal if they reach the adjacent dendritic shaft. Likely, such local calcium signals then act synergistically with the above-mentioned executive mechanisms (including complement deposition, which occurs in both in experimental and human neuroinflammatory conditions [32,45,46]) to induce immune-mediated synapse removal. The following aspects could contribute to such a collaborative interaction: The expression of eat-me signals in neurons could be directly regulated by calcium signals, as has been shown e.g. for the membrane exposure of phosphatidylserine [47] . Indeed, many aspects of developmental synapse pruning are activity-, and hence likely calcium-dependent, including complement-mediated synapse removal [44]. Furthermore, accumulating calcium could lead to a local de-stabilization of the cytoskeleton e.g. by the activation of calcium-dependent proteases [48] or phosphatases [12], which could facilitate subsequent spine removal – especially, if such remodelling became more widespread. This might explain the marked increase in spine loss observed once the calcium accumulation reached the dendritic shaft.

Importantly, irrespective of the precise mechanism of spine tagging and removal, we identify CSF1 signaling as a possible therapeutic intervention point, which could remedy cortical synapse loss. The notion that such cortical synapse loss is an important therapeutic target is supported by the prominent synaptic pathology present in the brain of MS patients [8,9,31] and the likely functional consequences that derive from it. The notion that CSF1 signaling may be an appropriate way to target this pathology in MS

is further supported by the targeted analysis of previously published single-nucleus RNA sequencing data [49] indicating that in the cortex of progressive MS patients CSF1-R is prominently expressed by microglial cells. In contrast, CSF1-R ligands are primarily expressed by glial cells (in the case of CSF1) and excitatory neurons (in the case of interleukin 34; **Supplementary Figure 11**).

However, one should keep in mind that a transient removal of preferentially excitatory inputs, as we observe here, could also have protective effects for neuronal health at least in the acutely inflamed gray matter. In this context it is interesting to note that we did not detect any obvious signs of increased neuronal stress in response to CSF1-R treatment (**Supplementary Figure 12**), arguing that at least this therapeutic modality did not inadvertently endanger neuronal survival. Moreover, the dose of CSF1-R inhibitor treatment that we employ here avoids microglia depletion. Such transient ablation of an essential CNS cell population generates divergent outcomes in chronic EAE models [26,50] and harbors unpredictable risks in a translational setting. Non-depleting CSF1-R-inhibition[25], in contrast, appears to have a two-pronged beneficial effect in the context of our c-MS model – affecting the peripheral and the central arm of the phagocyte response in parallel. On the one hand, such CSF1-R blockade reduces infiltration of $Ccr2^{pos}$ phagocytes into the CNS, which is prominent in our model, but also in gray matter of MS patients [7]. On the other hand, it reduces microglia-mediated synapse removal inside the CNS, which is another feature shared by our model and gray matter pathology in progressive MS [32]. Based on our transcriptomics analysis, these effects are orchestrated by locally activated phagocytes, which in response to CSF1-R blockade alter their disease-associated phenotype, reduce the chemoattraction of peripheral phagocytes and down-regulate their capacity for synapse removal, suggesting a 'paralysis' of detrimental executive function. In summary, our data imply that the progressive phase of MS, which appears refractory to current 'peripheral' immunomodulatory therapies [2], might be amenable to a suitable strategy for CNS-targeted immunomodulation.

ACKNOWLEDGEMENTS

We would like to thank A. Schmalz, M. Adrian, L. Schödel, B. Fiedler and Y. Hufnagel for excellent technical assistance, D. Matzek, B. Stahr, N. and M. Budak for animal husbandry. We acknowledge the Core Facility Flow Cytometry at the Biomedical Center, Ludwig-Maximilians-Universität München, for providing equipment, services and expertise.

This project was supported by the Deutsche Forschungsgemeinschaft (DFG) via TRR 274/1 2020 (Projects B03, C02, C05, Z01, Z02 – ID 408885537). Work in M.K.'s laboratory is further financed through grants from the DFG (TRR128, Project B10 and B13, the European Research Council under the European Union's Seventh Framework Program, FP/2007-2013; ERC Grant Agreement n. 310932), the German Federal Ministry of Research and Education (BMBF; Competence Network Multiple Sclerosis), the "Verein Therapieforschung für MS-Kranke e.V.". Part of this work was further supported by a research grant from Sanofi to M.K. Work in T.M.'s lab is supported by the DFG (CIPSM EXC114, CRC870, Mi 694/8-1), the German Center for Neurodegenerative Diseases (DZNE) and the European Research Council (FP/2007-2013; ERC Grant Agreement n. 616791). M.K. and T.M. are further supported by the DFG through a common grant (Ke 774/5-1/Mi 694/7-1) and the Munich Center for Systems Neurology (SyNergy EXC 2145; Project ID 390857198). M.K. and M.J. were supported by a grant from the German National MS Society (DMSG). M.K., D.M., and T.M. were supported through grants from the Gemeinnützige Hertie Stiftung. Work in D.M.`s laboratory is further supported by the Swiss National Science Foundation (No. PP00P3_152928 and No. 310030_185321), the Klaus-Tschira Foundation, Helmut Horten Foundation and the Gebert-Rüf Foundation and European Research Council (ERC Grant Agreement n. 865026. Work in F.W.`s laboratory was financed through the DFG (CRC889, Project B6; CRC1286 Project C2), BMBF (01GQ0922), GIF (906-17.1/2006), VW foundation (ZN2632), BCCN (01GQ1005B) and the Max Planck Society. N.S. is supported by a DFG research grant

(Sn 149/1-1; Project ID 426715780) and the Hertie Network of Excellence in Clinical Neuroscience (P1200019). A-M.S. and T.N. were supported by the "*Förderprogramm für Forschung und Lehre*" at Ludwig-Maximilians University Munich.

AUTHOR CONTRIBUTIONS

M.K., D.M. and T.M. conceived and designed the experiments. M.J., T.J., M.Kr. and D.M. established and characterized the c-MS model. M.J., A-M.S., E.M.U.G., V.K.-J., I.W. and S.S. performed and evaluated cortical pathology in situ. A-M.S., T.N., and E.M.U.G. performed and evaluated *in vivo* calcium imaging of spines and dendrites. N.S., J.D.F.W. and F.W. performed and/or analysed neuronal activity patterns *in vivo*. N.S. performed electron microscopy analysis. R.P. and J.G. performed data analysis. D.E. and E.B. performed bioinformatics analysis. M.J. and E.B. performed flow cytometry experiments. N.H., L.W. and D.O. developed and characterized the CSF1-R antagonist. M.J., A-M.S., N.S., D.M., T.M. and M.K. wrote the paper.

REFERENCES

1. Reich, D. S., Lucchinetti, C. F. & Calabresi, P. A. Multiple sclerosis. *New England Journal of Medicine* **378**, 169–180 (2018).

2. Mahad, D. H., Trapp, B. D. & Lassmann, H. Pathological mechanisms in progressive multiple sclerosis. *The Lancet Neurology* **14**, 183–193 (2015).

3. Damjanovic, D. *et al.* Hippocampal and deep gray matter nuclei atrophy is relevant for explaining cognitive impairment in MS: A multicenter study. *Am. J. Neuroradiol.* **38**, 18–24 (2017).

4. Eshaghi, A. *et al.* Deep gray matter volume loss drives disability worsening in multiple sclerosis. *Ann. Neurol.* **83**, 210–222 (2018).

5. Scalfari, A. *et al.* The cortical damage, early relapses, and onset of the progressive phase in multiple sclerosis. *Neurology* **90**, e2099–e2106 (2018).

6. Peterson, J. W., Bö, L., Mörk, S., Chang, A. & Trapp, B. D. Transected neurites, apoptotic neurons, and reduced inflammation in cortical multiple sclerosis lesions. *Ann. Neurol.* **50**, 389–400 (2001).

7. Lagumersindez-Denis, N. *et al.* Differential contribution of immune effector mechanisms to cortical demyelination in multiple sclerosis. *Acta Neuropathol.* **134**, 15–34 (2017).

8. Jürgens, T. *et al.* Reconstruction of single cortical projection neurons reveals primary spine loss in multiple sclerosis. *Brain* **139**, 39–46 (2016).

9. Albert, M. *et al.* Synaptic pathology in the cerebellar dentate nucleus in chronic multiple sclerosis. *Brain Pathol.* **27**, 737–747 (2017).

10. Rose, T., Jaepel, J., Hübener, M. & Bonhoeffer, T. Cell-specific restoration of stimulus preference after monocular deprivation in the visual cortex. *Science (80-.).* **352**, 1319–1322 (2016).

11. Xu, T. *et al.* Rapid formation and selective stabilization of synapses for enduring motor memories. *Nature* **462**, 915–919 (2009).

12. Kuchibhotla, K. V. *et al.* Aβ Plaques lead to aberrant regulation of calcium homeostasis in vivo resulting in structural and functional disruption of neuronal networks. *Neuron* **59**, 214–225 (2008).

13. Merlini, M. *et al.* Fibrinogen induces microglia-mediated spine elimination and cognitive impairment in an Alzheimer's disease model. *Neuron* **101**, 1099-1108.e6 (2019).

14. Merkler, D., Ernsting, T., Kerschensteiner, M., Brück, W. & Stadelmann, C. A new focal EAE model of cortical demyelination: Multiple sclerosis-like lesions with rapid resolution of

inflammation and extensive remyelination. *Brain* **129**, 1972–1983 (2006).

15. Gardner, C. *et al.* Cortical grey matter demyelination can be induced by elevated pro-inflammatory cytokines in the subarachnoid space of MOG-immunized rats. *Brain* **136**, 3596–3608 (2013).

16. Lodygin, D. *et al.* β-Synuclein-reactive T cells induce autoimmune CNS grey matter degeneration. *Nature* **566**, 503–508 (2019).

17. Magliozzi, R. *et al.* Inflammatory intrathecal profiles and cortical damage in multiple sclerosis. *Ann. Neurol.* **83**, 739–755 (2018).

18. Lucchinetti, C. F. *et al.* Inflammatory cortical demyelination in early multiple sclerosis. *N. Engl. J. Med.* **365**, 2188–2197 (2011).

19. Dana, H. *et al.* Thy1-GCaMP6 transgenic mice for neuronal population imaging in vivo. *PLoS One* **9**, e108697 (2014).

20. Schain, A. J., Hill, R. A. & Grutzendler, J. Label-free in vivo imaging of myelinated axons in health and disease with spectral confocal reflectance microscopy. *Nat. Med.* **20**, 443–449 (2014).

21. Siffrin, V. *et al.* In vivo imaging of partially reversible Th17 cell-induced neuronal dysfunction in the course of encephalomyelitis. *Immunity* **33**, 424–436 (2010).

22. Witte, M. E. *et al.* Calcium influx through plasma-membrane nanoruptures drives axon degeneration in a model of multiple sclerosis. *Neuron* **101**, 615-624.e5 (2019).

23. Thestrup, T. *et al.* Optimized ratiometric calcium sensors for functional in vivo imaging of neurons and T lymphocytes. *Nat. Methods* **11**, 175–182 (2014).

24. Yamasaki, R. *et al.* Differential roles of microglia and monocytes in the inflamed central nervous system. *J. Exp. Med.* **211**, 1533–1549 (2014).

25. Hagan, N. *et al.* CSF1R signaling is a regulator of pathogenesis in progressive MS. *Cell. Death. Dis.* **11**, 904 (2020).

26. Nissen, J. C., Thompson, K. K., West, B. L. & Tsirka, S. E. Csf1R inhibition attenuates experimental autoimmune encephalomyelitis and promotes recovery. *Exp. Neurol.* **307**, 24–36 (2018).

27. Olmos-Alonso, A. *et al.* Pharmacological targeting of CSF1R inhibits microglial proliferation and prevents the progression of Alzheimer's-like pathology. *Brain* **139**, 891–907 (2016).

28. Huang, D., Wang, J., Kivisakk, P., Rollins, B. J. & Ransohoff, R. M. Absence of monocyte chemoattractant protein 1 in mice leads to decreased local macrophage recruitment and antigen-

specific T helper cell type 1 immune response in experimental autoimmune encephalomyelitis. *J. Exp. Med.* **193**, 713–725 (2001).

29. Krasemann, S. *et al.* The TREM2-APOE pathway drives the transcriptional phenotype of dysfunctional microglia in neurodegenerative diseases. *Immunity* **47**, 566-581.e9 (2017).

30. Calabrese, M. *et al.* Cortical lesion load associates with progression of disability in multiple sclerosis. *Brain* **135**, 2952–2961 (2012).

31. Dutta, R. *et al.* Demyelination causes synaptic alterations in hippocampi from multiple sclerosis patients. *Ann. Neurol.* **69**, 445–454 (2011).

32. Michailidou, I. *et al.* Complement C1q-C3-associated synaptic changes in multiple sclerosis hippocampus. *Ann. Neurol.* **77**, 1007–1026 (2015).

33. Terry, R. D. *et al.* Physical basis of cognitive alterations in alzheimer's disease: Synapse loss is the major correlate of cognitive impairment. *Ann. Neurol.* **30**, 572–580 (1991).

34. Busche, M. A. *et al.* Clusters of hyperactive neurons near amyloid plaques in a mouse model of Alzheimer's disease. *Science (80-.).* **321**, 1686–1689 (2008).

35. Šišková, Z. *et al.* Dendritic structural degeneration is functionally linked to cellular hyperexcitability in a mouse model of alzheimer's disease. *Neuron* **84**, 1023–1033 (2014).

36. Marinković, P. *et al.* In vivo imaging reveals reduced activity of neuronal circuits in a mouse tauopathy model. *Brain* **142**, 1051–1062 (2019).

37. Rocca, M. A. *et al.* Default-mode network dysfunction and cognitive impairment in progressive MS. *Neurology* **74**, 1252–1259 (2010).

38. Kerschensteiner, M. *et al.* Remodeling of axonal connections contributes to recovery in an animal model of multiple sclerosis. *J. Exp. Med.* **200**, 1027–1038 (2004).

39. Ellwardt, E. *et al.* Maladaptive cortical hyperactivity upon recovery from experimental autoimmune encephalomyelitis. *Nat. Neurosci.* **21**, 1392–1403 (2018).

40. Jawaid, S. *et al.* Alterations in CA1 hippocampal synapses in a mouse model of fragile X 59. Hong, S. *et al.* Complement and microglia mediate early synapse loss in Alzheimer mouse models. *Science (80-.).* **352**, 712–716 (2016).

41. Vasek, M. J. *et al.* A complement-microglial axis drives synapse loss during virus-induced memory impairment. *Nature* **534**, 538–543 (2016).

42. Di Liberto, G. *et al.* Neurons under T cell attack coordinate phagocyte-mediated synaptic

stripping. *Cell* **175**, 458-471.e19 (2018).

43. Murphy, K. L. *et al.* Synaptic alterations and immune response are sexually dimorphic in a non-pertussis toxin model of experimental autoimmune encephalomyelitis. *Exp. Neurol.* **323**, 113061 (2020).

44. Hong, S. & Stevens, B. Microglia: Phagocytosing to clear, sculpt, and eliminate. *Dev. Cell* **38**, 126–128 (2016).

45. Hammond, J. W. *et al.* Complement-dependent synapse loss and microgliosis in a mouse model of multiple sclerosis. *Brain. Behav. Immun.* **87**, 739–750 (2020).

46. Werneburg, S. *et al.* Targeted complement inhibition at synapses prevents microglial synaptic engulfment and synapse loss in demyelinating disease. *Immunity* **52**, 167-182.e7 (2020).

47. Tufail, Y. *et al.* Phosphatidylserine exposure controls viral innate immune responses by microglia. *Neuron* **93**, 574-586.e8 (2017).

48. Andres, A. L. *et al.* NMDA Receptor activation and Calpain contribute to disruption of dendritic spines by the stress neuropeptide CRH. *J. Neurosci.* **33**, 16945–16960 (2013).

49. Schirmer, L. *et al.* Neuronal vulnerability and multilineage diversity in multiple sclerosis. *Nature* **573**, 75–82 (2019).

50. Tanabe, S., Saitoh, S., Miyajima, H., Itokazu, T. & Yamashita, T. Microglia suppress the secondary progression of autoimmune encephalomyelitis. *Glia* **67**, 1694–1704 (2019).

1

Fig. 1. Projection neurons lose excitatory synaptic input in a model of cortical multiple sclerosis

(**a**) Schematic of experimental design to measure spine density (c-MS model perfused at 3 and 14 days after intracortical cytokine injection; 'c-MS d3' and 'c-MS d14'). (**b**) MBP staining (white) and Iba-1 staining (magenta) in MOG immunized control (**left**) and c-MS model (**middle**, **right**). Demyelination and inflammation are observed both ipsilateral ('Ipsi'; **middle**) and contralateral ('Contra'; **right**) to the injection site. (**c**) Overview of *Thy1-GFP-M x BiozziABH x* cortex. (**d**) Confocal reconstruction of layer III and layer V pyramidal neurons (boxes in **c**). (**e**) Deconvoluted apical dendrite segments (typical locations on dendrites shown by boxes in **d**). (**f, g**) Spine density in apical dendrite of (**f**) layer III neurons (n=13 Ctr and n=15 c-MS d3 neurons from n=6 mice per group) and (**g**) layer V neurons (n=21/28 neurons from n=7/8 mice; mean ± SEM; two-way RM ANOVA). **(h)** Spine density of layer V dendrites over the course of c-MS (n=46 Ctr, n=62 c-MS d3 and n=52 c-MS d14 dendritic stretches from n=7/8/9 mice; mean ± SEM; one-way ANOVA followed by Bonferroni's multiple comparisons test; $F_{2,157}$=10, p<0.0001). **(i)** Electron micrographs (EM) of sham injected (**left**) and c-MS d3 (**right**) layer I (presynaptic compartment in red; postsynaptic in green; inset in **middle** shows detail boxed on left; synaptic cleft, white arrowhead; postsynaptic densities, black arrowheads). (**j**) EM-based quantification of synapse density in layer I in sham injected and c-MS animals (d3: n=4, sham; n=4 c-MS; d10 n=5 sham, n=3 c-MS mice; mean ± SEM; unpaired t-test). (**k**) Confocal analysis of excitatory pre- (vGlut1; red) and postsynaptic (Homer-1; green) synapses in immunostained cortical layer II-IV of control (**left**) and c-MS d3 mice (**right**; inset shows 2.5-fold magnification). (**l)** Inhibitory pre- (GAD 65/67; red) and postsynaptic (Gephyrin; green) synapses, same arrangement as **k**. (**m, n**) Quantification of (**m**) excitatory and (**n**) inhibitory synapse density (n=4 Ctr and n=12 c-MS d3 mice per group; mean ± SEM; unpaired t-test). (**o**) Ratio of excitatory to inhibitory synapse densities calculated from m, n (mean ± SEM; unpaired t-test). Scale bars in **b**, 50 µm; **c**, 100 µm; **d**, 20 µm; **e,** 1 µm **i**, 1 µm, **k** and **l**: 2 µm. Display range is adjusted for images in panels **b**-**e** uniformly in each panel. Deconvoluted images are used in

panel **e**. In panels **k**, **l** mean intensity and standard deviation (SD) of the background was calculated based on 5 ROIs and mean+3SD was used to threshold the image for display purposes. Abbreviations: Ctr: Control; c-MS: cortical MS model; dX: perfused at day X; Ipsi: Ipsilateral to cytokine injection; Contra: Contralateral to cytokine injection. *** P<0.001, ** P<0.01, *P<0.05.

Fig. 2. Neurons are silenced in a model of cortical multiple sclerosis

(**a**) Schematic showing experimental design for longitudinal *in vivo* imaging of neuronal activity in layer II/III somatosensory neurons in the c-MS model, using GCaMP6s as calcium indicator delivered via viral gene transfer (AAV1.hSyn1.mRuby2.GCaMP6s). (**b**) *In vivo* multiphoton imaging of a layer II/III neurons over the course of cortical inflammation through a cranial window. **From left to right,** respectively: before cytokine injection ('Baseline MOG'), 3 days ('c-MS d3'), 10 days ('c-MS d10') and 17 days ('c-MS d17') after cytokine injection. **Top**: Grayscale images of GCaMP6s channel masked and color-coded for cytoplasmic Ca^{2+} events per minute. **Bottom**: Representative Ca^{2+} activity traces displayed as delta f/f for the neurons marked in the left panel. (**c**) Cumulative plots of the neuronal activity for the entire population of neurons for each selected timepoint over the course of the c-MS model (**top**) and for sham injected animals (**bottom**). **Inserts**: Mean neuronal activity normalized to baseline for each timepoint shown as (n=4 sham injected and n=5 c-MS mice, mean ± SEM; RM One-way ANOVA followed by Dunnett's multiple comparison test; $F_{1.916,\ 7.662}$=6.38, p=0.0241). (**d**) Heat map representation of the activity levels of single neurons over the course of c-MS (**left**) and for sham injected animals (**right**). Scale bar in **b**, 20 µm. *P<0.01

Fig. 3. Resilience of neuronal circuit structure in a model of cortical multiple sclerosis

(**a**) **Left:** Fold activity change for neurons showing > 0.5 Ca^{2+} events per minute between c-MS d3 and baseline (b-) MOG (orange), c-MS d17 and b-MOG (light orange) and sham d17 and baseline timepoints (grey; n=464/464/354 cells, respectively; dashed lines: median, thin dashed lines quartiles; Kruskal-Wallis test followed by Dunn's multiple comparison test). **Right**: Binned activity change between baseline and 17 days post injection in sham injected and c-MS mice (n=4 sham injected and n=4 c-MS mice). (**b, c**) Representative pairwise correlations of individual neuronal activity (c_{signal}) in a somatosensory cortex area with 55 neurons after sham injection (in **b**) and over the course of the c-MS model (in **c**). (**d**) Schematic to illustrate session-wise similarity (r_{signal}) calculation with c_{signal} structure at every timepoint (d3, d10 and d17) reported to before cytokine injection (baseline MOG) in the c-MS model or to baseline in sham injected control. r_{signal} is calculated from the average of the multiple comparison based on three repetitive sessions at each timepoint (**e**) Cubic polynomial fit of the average inter-timepoint similarity over the course of the c-MS model and in comparison with sham injected mice (thick orange and black lines). The 5th and 95th percentiles of the sham subsets are represented in dashed black and the max and min in solid thin black. Data shown as mean ± SEM (n=4 control and n=4 c-MS mice, polynominal analysis followed by Mann-Whitney test for the differences of the distributions between c-MS and sham injected mice). ***P<0.001, *P<0.05.

Fig. 4. Localized calcium accumulations prime spines for removal

(**a**) Schematic of *in vivo* imaging of spine Ca^{2+} levels in the c-MS model using the FRET-based genetically encoded calcium indicator Twitch2b delivered via viral gene transfer (AAV1.hSyn1.Twitch2b). (**b**) Timecourse of spine density in apical tuft dendrites of *Thy1-GFP-M x BiozziABH* mice quantified *in situ* in the c-MS model (control, 'Crt', n=5 mice; c-MS d1, n=8 mice; c-MS d2, n=7 mice and c-MS d3, n=7 mice; mean ± SEM; one-way ANOVA followed by Bonferroni's multiple comparisons test, $F_{3,23}$=7.415, p=0.0012). (**c**) *In vivo* multiphoton projection images of apical tuft dendrites with spines and their Ca^{2+} levels in healthy control ('Ctr'; **top**) and acute (d3) cortical MS model ('c-MS'; **bottom**). Grayscale images of YFP channel, ratiometric (YFP/CFP) images masked and color-coded for cytoplasmic Ca^{2+}. (**d**) Ca^{2+} concentration of single spines in healthy ('Ctr') and c-MS model ('c-MS d3') mice, plotted as YFP/CFP channel ratios (dashed line representing high Ca^{2+} threshold, 3SD above control mean) **Top:** Percentage of spines per animal with high Ca^{2+}, shown as mean ± SEM (tested per animal in n=8 control and n=17 c-MS mice, Mann-Whitney U test). (**e**) **Left:** Representative calcium activity traces obtained using resonant scanner-based imaging, displayed as YFP/CFP normalized channel ratios over time in relation to high Ca^{2+} threshold (dashed lines). **Right:** mean baseline Ca^{2+} of single spines (normalized to control mean) shown in relation to their calcium activity (spiking frequency x min^{-1}), dashed yellow line representing high Ca^{2+} threshold. (**f**) Multiphoton time-lapse images in healthy control and c-MS mice (d2, d3) represented as a grayscale images of YFP channel and ratiometric (YFP/CFP) images masked and color-coded for cytoplasmic Ca^{2+}. **Top:** stable control low Ca^{2+} spines. **Middle:** high Ca^{2+} spine (**left**, yellow arrow head) disappearing after 2h (**right,** dashed arrow head). **Bottom:** Spine (**left**, white arrow head) increasing volume and Ca^{2+} after 2h (**right**, yellow arrow head) next to neighboring spine with high Ca^{2+} disappearing after 2h (**right**, dashed arrow head). Gamma 1.2 for grayscale images. (**g**) Spine fate over a 2 hour imaging timeperiod according to baseline Ca^{2+} concentration at t=0h (in mean +x SD of healthy controls) in healthy mice (**left**, Ctr) and c-MS mice (**middle**). **Right**: Percentage of high Ca^{2+} spines (3SD above control mean) lost within 2

hours according to their individual peri-spine dendritic Ca^{2+} concentration (high vs. low, as defined by 3SD above the mean calcium levels in control dendrites; Fisher's exact test, n=24 spines with low dendrite calcium, n=8 spines with high dendrite calcium). (**h**) Ca^{2+} levels (as YFP/CFP ratios normalized to control mean, dashed yellow line representing high Ca^{2+} threshold) of single spines over 2 h in c-MS (d2, d3) mice. Dashed, orange lines represent high Ca^{2+} spines disappearing within 2 h. (**i**) Percentage of low Ca^{2+} spines strongly increasing Ca^{2+} over time (**left)** and percentages of high Ca^{2+} spines reducing Ca^{2+} over time (**middle**), or getting lost (**right**) in c-MS mice with (blue) or without (orange) local application of 50 mM EGTA (tested per animal, n=11 c-MS mice without EGTA, n=10 c-MS mice with EGTA, one-tailed t-tests). Scale bars in c, 10 µm; f, 5 µm. **P < 0.01, *P<0.05.

Fig. 5. Mononuclear phagocytes remove synapses

(**a**) Orthogonal view of a $CX_3CR\text{-}1^{GFP}$ cell (magenta) showing a Synapsin-1 inclusion (cyan, **left**) colocalized with LAMP1 staining (white, **right**) suggesting removal of synapses by CNS resident microglial cells. (**b**) Orthogonal view of a $Ccr2^{RFP}$ cell (magenta) showing Synapsin-1 inclusion (cyan), suggesting removal of synapses by blood-derived mononuclear phagocytes. (**c**) Quantification of reconstructed Synapsin-1 positive spheres and Synapsin-1/LAMP1 double positive spheres inside $CX_3CR\text{-}1^{GFP}$ cells analysed in *$CX_3CR\text{-}1^{GFP}$ x BiozziABH* mice (n=50 cells from 4 healthy control mice and 50 cells from 5 c-MS d3 mice; mean ± SEM; unpaired t-test). (**d**) **Left:** 3D reconstruction of the cell in **a** (magenta) and its Synapsin-1 inclusions (cyan) with Imaris software. **Right:** Electron micrograph of a phagocyte (violet) in cortical layer I during the acute phase of c-MS. **Insert**: Synaptic components (cyan) in a degradative compartment of the phagocyte. (**e**) Quantification of reconstructed Synapsin-1 positive spheres and Synapsin-1/LAMP1 double positive spheres inside $Ccr2^{RFP}$ cells (n=50 cells from 5 c-MS d3 *$Ccr2^{RFP}$ x BiozziABH* mice mice; mean ± SEM). (**f**) Quantification of reconstructed spheres positive for postsynaptic markers and co-localizing with LAMP1 inside $CX_3CR\text{-}1^{GFP}$ cells analysed in *$CX_3CR\text{-}1^{GFP}$ x BiozziABH* mice (n=50 cells from 5 healthy control mice and 50 cells from 5 c-MS d3 mice treated with vehicle; mean ± SEM; unpaired t-test). (**g**) Quantification of reconstructed spheres positive for postsynaptic markers and co-localizing with LAMP1 inside $Ccr2^{RFP}$ cells (n=50 cells from 4 c-MS d3 *$Ccr2^{RFP}$ x BiozziABH* mice treated with vehicle; mean ± SEM). Scale bars in **a** and **b**, 5 µm; **d**, 2 µm. Abbreviations: Syn1: Synapsin-1; c-MS: cortical MS model; Ctr: Control; ND: No data. *** $P<0.001$, ** $P<0.01$.

Fig. 6. Blocking phagocyte entry and activation prevents synapse loss in the c-MS model

(**a**) Schematic timeline of treatment with CSF1-R inhibitor ('CSF1-R inhib') or vehicle in the c-MS model. (**b**) Representative images of deconvoluted apical dendritic stretches from layer V pyramidal neurons showing spines in c-MS d3 mice treated with vehicle (**left**) or CSF1-R inhibitor (**right**). (**c**) Spine density of apical dendritic stretches from layer V pyramidal neurons in c-MS d3 mice treated with vehicle or CSF1-R inhibitor (n=65/48 neurons from n=8/7 mice; mean ± SEM; unpaired t-test). The dotted line shows the average spine density in healthy control mice based on **Fig. 1g**. (**d, e**) Gating strategy for sorting cells based on CD45 and CD11b expression in brains of *Ccr2^{RFP} x BiozziABH* c-MS model mice treated with vehicle or CSF1-R inhibitor. (**d**) After separation of debris and doublets, live cells were further gated by CD45 and CD11b expression to identify mononuclear phagocytic cells. (**e**) CD45^{high} CD11b^{high} cells were further gated into two populations depending on the presence of Ccr2-^{RFP} positivity. (**f-h**) Volcano plot based on differentially expressed genes between CSF1-R inhibitor treatment vs. vehicle in CD45^{int} CD11b^{int} cells (**f**), CD45^{high} CD11b^{high} Ccr2^{pos} cells (**g**) and CD45^{high} CD11b^{high} Ccr2^{neg} cells (**h**). (**i**) Heatmap of treatment-affected genes associated with APOE signaling as measured in transcriptomic analysis of CD45^{high} CD11b^{high} Ccr2^{neg} cells (vehicle vs CSF1-R inhibitor treatment, n=5 and n=6 mice respectively). (**j**) Genes predicted by Ingenuity Pathway Analysis to be directly regulated by CSF1 signaling (p-value cutoff of 0.05 and fold change cutoff of -2) in CD45^{high} CD11b^{high} Ccr2^{neg} cells (vehicle vs treatment, n=5/6 mice) (**k**) Quantification of CX$_3$CR-1^{GFP} cells in cortical sections of c-MS d3 *CX$_3$CR-1^{GFP} x BiozziABH* mice treated with vehicle or CSF1-R inhibitor (n=9 mice per group; mean ± SEM; unpaired t-test). (**l**) Quantification of Iba-1^{positive} CX$_3$CR-1^{GFP} negative cells (infiltrating mononuclear cells) in c-MS d3 *CX$_3$CR-1^{GFP} x BiozziABH* mice treated with vehicle or CSF1-R inhibitor (n=9 mice per group; mean ± SEM; unpaired t-test). (**m**) Effects on synapse removal by CX$_3$CR-1^{GFP} cells in c-MS d3 *CX$_3$CR-1^{GFP} x BiozziABH* mice. **Left:** Delta (Δ) of the LAMP1 positive volume proportion per CX$_3$CR-1^{GFP} cell volume as percentage of vehicle treated group. 'Delta'

refers to subtraction of average volume of healthy controls (derived from Ctr group images used in **Fig. 5c,f**) from vehicle or CSF1-R inhibitor treated c-MS mice (n=150 cells analysed from 5 mice per group; mean ± SEM; unpaired t-test. **Right:** Delta (Δ) of the number of Synapsin-1/LAMP1 and Homer-1/LAMP1 double positive spheres per $CX_3CR\text{-}1^{GFP}$ cells in c-MS d3 mice treated with vehicle or CSF1-R inhibitor. Delta refers to subtraction of number of spheres of healthy control (data derived from **Fig. 5c,f**) from vehicle or CSF1-R inhibitor treated c-MS mice (n=50 cells analysed from 5 mice in each group; mean ± SEM; unpaired t-test; data for Homer-1/LAMP1 vehicle treated group replotted from **Fig. 5f**). (**n**) Effects on synapse removal by $Ccr2^{RFP}$ cells in c-MS d3 *$Ccr2^{RFP}$ x BiozziABH* mice **Left:** LAMP1 positive volume per $Ccr2^{RFP}$ cell volume as percentage of vehicle treated group (n=150 cells from 4 vehicle-treated and 5 CSF1-R inhibitor-treated mice; mean ± SEM; unpaired t-test). **Right:** Number of Synapsin-1/LAMP1 and Homer-1/LAMP1 double positive spheres per $Ccr2^{RFP}$ cells in c-MS d3 mice treated with vehicle or CSF1-R inhibitor (n=50 cells analysed from 4 vehicle-treated mice and 5 CSF1-R inhibitor-treated mice; mean ± SEM; unpaired t-test; data for Homer-1/LAMP1 vehicle treated group replotted from **Fig. 5g**). (**o**) *In vivo* ratiometric projection images of representative dendrites and spines color-coded for cytoplasmic Ca^{2+} calcium levels of vehicle (**left**) and CSF1-R inhibitor (**right**) treated mice. (**p**) Percentage of spines with high Ca^{2+} after treatment with vehicle or CSF1-R inhibitor (n=9 mice per group; mean ± SEM; unpaired t-test). Scale bar in **b**, 2 µm ; **o**, 5 µm *** P<0.001, **P<0.01,*P<0.05.

ONLINE METHODS

Experimental Models

Transgenic animals

All experiments were performed on animals with a F1 and F2 background of C57BL/6 and BiozziABH (strain designation BiozziABH/RijHsd, Harlan Laboratories), crossbred in our animal facilities. To assess dendritic and spine pathology *in situ*, we used *Thy1-GFP-M x BiozziABH* mice (derived from *Tg(Thy1-EGFP)MJrs/J*, gift from Joshua Sanes and Jeff Lichtman, Harvard University). To address phagocyte activation, infiltration and synaptic uptake, we used *Ccr2^{RFP} x BiozziABH* animals (derived from *B6.129(Cg)-Ccr$_2$tm2.1Ifc/J*, Jackson Laboratory) and *CX$_3$CR-1^{GFP} x BiozziABH* mice (*B6.129P-Cx$_3$cr-1tm1Litt/J*, Jackson Laboratory) or a F2 cross-breeding of both lines. For viral labelling, either *Ccr$_2^{RFP}$ x BiozziABH* or *C57BL/6J x BiozziABH* were used. To assess calcium activity in layer V pyramidal neurons, we used *Thy1-GCamP6f x BiozziABH* mice (derived from *C57BL/6J- Tg(Thy1-GCaMP6f)GP5.5Dkim/J*, Jackson Laboratory). Mice were housed in individual ventilated cage systems under a 12:12 light/dark cycle, at a temperature of 22° ± 2°C and 55% ± 10% relative humidity with complete feed and water ad libitum. They were housed in social groups of a maximum of 5 mice in each standard housing cage and bedding. The cages were provided with enrichment consisting of play tunnels, nestlets to be used as nesting material and a red plastic mouse house. For husbandry, one male was housed with one or two females. Mice were weaned at postnatal day 21. Both female and male animals were included in experiments. All animal experiments were performed in accordance with regulations of the relevant animal welfare acts and protocols approved by the respective regulatory bodies.

Cortical multiple sclerosis model (c-MS)

Adult mice (6 - 14 weeks of age) were first induced with EAE as previously described. In short, we immunized animals subcutaneously under ketamine-xylazine anesthesia (KX, 87 mg/kg + 13 mg/kg) with 200 µl of an emulsion containing 30 µg of purified recombinant rat myelin oligodendrocyte

glycoprotein (MOG, N1-125, expressed in E. coli) and complete Freund's adjuvant, consisting of incomplete Freund's adjuvant (Sigma Aldrich, F5506) and 10 mg/ml mycobacterium tuberculosis H37 Ra (BD Difco, 231191). Pertussis toxin (200 ng, Sigma Aldrich, P7208) was administered intraperitoneally on day 0 and day 1 after immunization. The immunization procedure was repeated after 1 week. To evoke cortical lesions, we injected 2 µl of a cytokine mix of 0.25µg/µl recombinant mouse TNF-α (R&D Systems, 410-MT/CF) and 750 U/µl recombinant murine IFN-γ (Peprotech, 315-05) in PBS/0.1% BSA intracortically (coordinates: 1.2 mm lateral, 0.6 mm caudal to bregma, depth 0.8 mm) under anesthesia with a combination of medetomidine-midazolam-fentanyl (MMF, 0.5 mg/kg + 5 mg/kg + 0.05 mg/kg) 3 weeks after initial immunization. Mice were given buprenorphine (0.05 - 0.1 mg/kg) for analgesia on the days following the surgery. For all experimental animals, we assessed animal weight daily and assigned a score according to the severity of neurological deficits using an established EAE scoring scale that primarily monitors locomotor deficits caused by spinal white matter lesions: 0, no detectable clinical signs; 0.5, partial tail weakness; 1, tail paralysis; 1.5, gait instability or insecurity in walking; 2, hind limb paresis; 2.5, hind limb paresis with partial dragging; 3, hind limb paralysis; 3.5, hind limb paralysis and forelimb paresis; 4, hind limb and forelimb paralysis; 5, death. As expected for the c-MS induction protocol [18], most mice did not develop severe systemic EAE symptoms under our immunization protocol. Mice without obvious clinical signs of systemic EAE were also included in the study. We did not observe any obvious correlation between the EAE score and cortical spine loss (cf. **Supplementary Figure 1**).

Cranial window surgery

To gain optical access to the animal cortex to monitor neuronal activity over time and to assess *in vivo* calcium levels of dendrites and spines upon acute cortical inflammation, we performed a craniotomy and implanted a cranial window above the somatosensory cortex of the animals as previously described [72]. In brief, the mice were anaesthetized with MMF intraperitoneally. Craniotomy was performed using

a 0.5 mm stainless steel drill head (Meisinger, 310104001001005). For chronic imaging of neuronal activity, 0,5 µl of 10^{12} AAV1.hSyn.mRuby2.GSG.P2A.GCaMP6s (Addgene, 50942-AAV1) was injected 0.3 mm deep in the somatosensory cortex before sealing with a 4 mm cover class using dental cement. The labeled layer II/III neurons were predominantly excitatory (96.6 ± 0.6%, GAD67 immunostaining negative, mean ± SEM, 1447 neurons from 4 mice analysed). Mice were given buprenorphine (0.05 - 0.1 mg/kg) for analgesia every 12 h on the days following surgery. Under these conditions, no increase in cellular toxicity due to viral burden was observed throughout the entire experiment timeline. Animals were first imaged 28 days after implantation of chronic cranial windows.

For acute *in vivo* imaging of baseline calcium levels of dendrites and spines, 0,5 µl of 10^{12} AAV1.hSyn1.Twitch2b.WPRE.SV40 (Addgene, 100040-AAV1) was injected 0.7 mm deep into the somatosensory cortex, 10d before the imaging timepoint. Analgesia was applied after surgery as described above. On the imaging day, acute cranial window implantation was performed as stated above. To improve imaging quality and before application of EGTA, the dura mater was carefully removed using fine forceps (Dumont #5, Fine Science Tools, 91150-20). In cases of application of EGTA, cover glasses were not fully sealed, leaving a flow-through channel for the treatment solution to reduce manipulation.

Application of pharmacologicals

The c-MS model was induced as described above and animals were treated daily from the day of cytokine injection until perfusion (four days) with 25 mg/kg intraperitoneal injection of vehicle or the novel CSF1-R inhibitor compound (Sanofi). Two groups of age matched healthy controls received the same treatments. Analysis of spine density in dendritic stretches between healthy controls (n=30), healthy controls treated with vehicle (n=40) and healthy controls treated with CSF1-R inhibitor (n=30) did not reveal any significant changes (one-way ANOVA followed by Bonferonni's multiple comparisons test).

Method Details

Immunohistochemical stainings

Mice were transcardially perfused with 4% (wt/vol) paraformaldehyde in phosphate buffered saline and after 12-24h post-fixation embedded in paraffin. Axon density was determined by Bielschowsky silver staining. Deparaffinized tissue sections were washed with distilled water and subsequently incubated in 20% silver nitrate solution for 20 min, followed by another washing step. Sections were incubated in 20% silver nitrate solution containing 5% ammonium hydroxide for 15 min in the dark. Sections were transferred in 0.6% ammonium hydroxide and swayed. 1/35 volume of the developer solution was added to the 20% silver nitrate solution containing 5% ammonium hydroxide while stirring. Subsequently the sections were transferred into the solution and developed until the color of the sections turned brown. Following washing in distilled water, sections were incubated in 2% sodium thiosulfate solution for 2 min.

To stain for CD3, CD4, CD8, Mac-3 and c-Jun we performed antigen retrieval of paraffin-embedded sections by treating rehydrated tissue sections for 30 s at 125 °C under pressure (20-22 psi) in 1x citrate buffer (pH = 6) in a Pascal pressure chamber. After cooling-down, antigen-retrieved sections were washed in distilled water. Sections were then washed and blocked with peroxidase blocking solution (Dako, S2023) for 5 min. After two washing steps, sections were treated with the primary antibodies directed against CD3 (1:100, Dako, A0452), CD4 (1:400, Cell Signaling, 25229), CD8 (1:5000, Ebioscience, 14-0808-82), Mac-3 (1:200, Biolegend, 108502), and c-Jun (1:300, Cell Signaling, 9165). For the stainings using rat antibodies, we performed a Fab fragment block against mouse IgG (1:100. JIR, 115-007-003) to reduce unspecific bindings. After overnight incubation at 4° and wash, Impress HRP anti-rat IgG (Vector, MP7444) or Impress HRP anti-rabbit Ig G (Vector, MP7451) was added to the slides for 30 min. Subsequently, after two washing steps, the antibody binding was visualized using a DAB solution (Dako, K3468). To evaluate presence of c-Fos, paraffin embedded blocks were cut,

deparaffinized, rehydrated and underwent antigen retrieval with Pascale Citrate pH 6.0. Tissue was incubated with a primary anti-c-Fos antibody (1:1000, Synaptic Systems, 226 005) and subsequently incubated with a biotinylated anti-guinea pig secondary antibody (1:200, Vector, BA-7000) for 1h, followed by Streptavidin/HRP (Conjugate) (1:200, Dako, P0397) for 30 min. Tissue sections were washed with water followed by counterstaining with Mayer's hemalum solution (Merck, 109249).

MBP immunostaining was done using at room temperature in a humid chamber. Sections were washed in 1x wash buffer and blocked with Real peroxidase blocking solution (Dako, S2023) for 5 min. After two washing steps, sections were treated with rabbit anti-MBP antibody (1:1000, Dako, A0623) diluted in Dako Real antibody diluent for 1 h. After washing, Impress HRP anti-rabbit secondary antibody (vector, MP7451) was added for 30 min. Sections were washed twice and processed with DAB-containing developer solution (20 µl DAB chromogen + 1 ml DAB substrate buffer). Tissue sections were washed with water followed by counterstaining with Mayer's hemalum solution (Merck, 109249). All stained sections described above were dehydrated and mounted in Ultrakitt (Biosystems, 3921.0500) for imaging.

Immunofluorescence stainings

Mice were transcardially perfused with 4% (wt/vol) paraformaldehyde in phosphate buffered saline and the brains were post-fixed at 4°.

For evaluation of phagocyte activation and infiltration brains were post-fixed overnight, isolated, and 80-100 µm thick sections were cut using a vibratome. Sections were washed with PBS and blocked with 10% goat serum (GS) in 0.5% (vol/vol) Triton X-100 in PBS (T-PBS) and then incubated overnight with rabbit anti-Iba-1 (1:300, Wako, 019-19741) and rat anti-MHC II (I-A/I-E) (1:300, BD Biosciences, 556999) antibodies in 1% GS in T-PBS at 4º C. Sections were visualized by incubating overnight with AlexaFluor 647 goat anti-rabbit (1:500, Invitrogen, A21244) and AlexaFluor 594 goat anti-rat (1:500,

Invitrogen, A11007) antibodies together with the Nissl-like nucleic acid stain NeuroTrace 435/455 (1:500, Invitrogen, N21479) in 1% GS in T-PBS.

For evaluation of presynapse phagocytosis, brains were post-fixed 4-6 h, isolated, and cut in 40 µm thick sections using a vibratome. Sections were washed with PBS and blocked with 10% GS in 0.1% T-PBS and then incubated overnight with rabbit anti-Synapsin-1 (1:500, Millipore, AB1543) and rat anti-LAMP1 (1:300, Biolegend, 121601) antibodies in 1% GS in 0.1% T-PBS at room temperature. Sections were visualized by incubating overnight with AlexaFluor 647 goat anti-rabbit (1:500, Invitrogen, A21244) and AlexaFluor 594 goat anti-rat (1:500, Invitrogen, A11007) or AlexaFluor 488 goat anti-rat (1:500, Invitrogen, A11006) antibodies in 1% GS in T-PBS.

For evaluation of postsynapse phagocytosis, brains were fixed for 4-6 h, isolated and left in 30% sucrose for 3 days. The brains were then embedded in Tissue-Tek O.C.T. medium (Sakura, 4583) and cut in 40 µm thick sections using a cryostat. Sections were washed with PBS and blocked with 20% GS in PBS and incubated overnight with rabbit anti-PSD95 (1:200, Invitrogen, 51-6900) and rat anti-LAMP1 (1:300, Biolegend, 121601) antibodies or for 36 h with guinea pig anti-Homer-1 antiserum (1:500, Synaptic Systems, 160004) and rat anti-LAMP1 antibody (1:300, Biolegend, 121601) in 10% GS 0.3% T-PBS. Sections were visualized by incubating for 4 h with AlexaFluor 647 goat-anti rabbit (1:500, Invitrogen, A21244) or AlexaFluor 647 donkey anti-guinea pig (1:500, Invitrogen, A11075) and AlexaFluor 594 goat anti-rat (1:500, Invitrogen, A11007) or AlexaFluor 488 goat anti-rat (1:500, Invitrogen, A11006) antibodies in 1% GS in T-PBS.

To evaluate the density of excitatory and inhibitory synapses, paraffin embedded blocks were cut, deparaffinized, rehydrated and underwent antigen retrieval with Pascale Citrate pH 6.0. Fab mouse block (1:100, JIR, 115-007-003) and FCS 10% in PBS were used for blocking. For analysis of excitatory synapses sections were incubated with mouse anti-vGlut1 (BNPI) (1:100, Santa Cruz, sc-377425) and

chicken anti-Homer-1 (1:500, Synaptic Systems, 160006) antibodies in Dako diluent overnight at 4°. Sections were visualized with AlexaFluor 555 goat anti-mouse IgG1 (1:200, Invitrogen, A21127) and AlexaFluor 647 goat anti-chicken IgY (1:200, Invitrogen, A21449) incubated for 1 h at room temperature. For analysis of inhibitory synapses the tissue section were incubated with mouse anti-GAD 65/67 (1:100, Santa Cruz, sc-365180) and mouse anti-Gephyrin (1:200, Santa Cruz, sc-25311) antibodies. Sections were visualized with AlexaFluor 555 goat anti-mouse IgG1 (1:100, Invitrogen, A21127) and AlexaFluor 647 goat anti mouse IgG2b (1:200, Invitrogen, A21241). DAPI was diluted 1:2000 in PBS and added to the secondary antibody solution.

To observe extends of demyelination and inflammation, 100 µm thick sections were cut using a vibratome. Section were treated for 15 minutes with cooled methanol in -20°. Sections were washed with PBS and blocked with 10% horse serum (HS) in 0.1% T-PBS and then incubated overnight with rabbit anti-MBP (1:200, Dako, A0623) and goat anti-Iba-1 (1:200, Abcam, ab5076) in 1% HS in T-PBS at room temperature. Sections were visualized by incubating overnight with AlexaFluor 647 donkey anti-rabbit (1:500, Invitrogen, A31573) and AlexaFluor 594 donkey anti-goat (1:500, Invitrogen, A11058) antibodies in 1% HS in T-PBS.

For the evaluation of excitatory and inhibitory neuronal fractions infected by AAV1.hSyn.mRuby2.GSG.P2A.GCaMP6s in the mice used in functional imaging, we perfused the animals as described above after the last imaging session. Brains were post-fixed for 12 h, isolated, and cut in 50 µm thick sections using a vibratome. Sections were first permeabilized in 2% T-PBS in room temperature overnight then blocked in 2% FCS, 2% fishgelatine, 2% BSA in PBS for 2 h at room temperature. Sections were then incubated overnight with mouse anti-GAD67 antibody (1:50, Millipore, MAB5406B), chicken anti-GFP (1:1000, Abcam, ab13970) antibodies in 10% blocking solution at 4º C

overnight. Stainings were visualized by incubating sections for 2 h with AlexaFluor-conjugated antibodies AlexaFluor 647 or AlexaFluor 488 (1:500, Invitrogen).

All sections were washed with PBS and mounted on slides using Vectashield (Vector Laboratories, H-1000).

Confocal microscopy

To image immunofluorescence stained tissue, we used upright confocal laser-scanning microscopes, FV1000 (Olympus) or SP8 (Leica), equipped with standard filter sets and laser lines. To reconstruct apical dendrites in *Thy1-GFP-M x BiozziABH* animals, a 60x/1.35 NA oil immersion UPLSAPO objective (Olympus) was used with a digital zoom of 3.5, Z-spacing of 200 nm and a pixel resolution of 75 nm pixel^{-1} to image 80-100 µm thick coronal brain sections. Averaging of two images was done by the Kalman method. To evaluate the density of excitatory and inhibitory synapses in *C57BL/6 x BiozziABH* mice similar imaging setting was used. To acquire images to study microglia numbers and activation based on MHC II staining, and infiltrating phagocytes based on Iba-1 staining 80-100 µm thick coronal brain sections of *CX$_3$CR-1^{GFP} x BiozziABH* mice were imaged with a 20x/0.85 NA oil immersion UPLSAPO objective (Olympus). To demonstrate extents of demyelination and inflammation sections were imaged with the same method in *C57BL/6J x BiozziABH* mice. To assess temporal and spatial characteristics of monocyte infiltration and microglial activation, 80 µm thick sections from *CX$_3$CR-1^{GFP} x BiozziABH* and *Ccr2^{RFP} x BiozziABH* mice were imaged with a 20x/0.75 NA oil immersion HC PL APO CS2 objective (Leica) and 1.0x zoom in tile scan mode. Overview scans were overlayed on a scan of neurotrace signal, imaged with a 20x/0.85 NA oil immersion UPLSAPO Objective (Olympus).

For the evaluation of synapse phagocytosis, 40 µm thick sections were imaged with a 40x/1.30 oil immersion HC PL APO CS2 objective (Leica), 3.0x zoom, Z-spacing of 200 nm and a pixel size of 97 nm.

In vivo imaging

For chronic *in vivo* imaging of neuronal activity, animals were first imaged 28 days after implantation of cranial windows. For this analysis, we compared mice, in which a c-MS model was induced with mice, which received only a cytokine injection (but no immunization) and sham-injected mice, which were not immunized and in which a similar volume of 0.1% BSA/PBS without cytokines was injected. On the imaging day, animals were anaesthetized starting with 2% isoflurane and then placed on the imaging stage and provided with a constant flow of 1-1.5% isoflurane for the rest of the imaging period. The physiological state of the animals was continuously monitored with a MouseOx system (Starr Life Science Corp) equipped with a thigh sensor for small animals. Imaging of neuronal activity was performed on 2-3 areas of layer II/III somatosensory cortex at 15Hz with a resonant scanner (Olympus MPE-RS) using a femto-second pulsed Ti:Sapphire laser (Mai Tai Insight DeepSee, Spectra-Physics) with a maximum power of 35mW at the back focal plane. Each area was imaged 3 times 5 minutes within 1 hour. A 25x/1.05 dipping cone water-immersion objective (Olympus) was used with a zoom of 1.5x and a pixel size of 660 nm pixel^{-1}.

To image cortical myelin (layer I) we performed spectral confocal reflectance microscopy (SCoRe) as described before [27]. We used 3 fixed wavelength lasers (488, 539 and 633) to generate the SCoRe signal (adjustable bandpass filter: 488/4 and 539/4: Olympus, as well as a fix bandpass filter 636/8 BrightLine HC). Imaging was performed within the first 70 µm of the somatosensory cortex above the imaged areas used for the activity recordings. A 40x/0.8 water- immersion objective (Olympus) was used with a zoom of 1.0x and a pixel size of 200 nm pixel^{-1}. Volume stacks penetrating 50-70 µm into the cortical layer I from the surface were acquired with a Z-spacing of 1 µm. A single plane from the stacks was used for each analysis. For acute *in vivo* imaging of calcium levels of dendrites and spines, animals were anaesthetized with a mixture of medetomidin (0.5 mg/kg), midazolam (5 mg/kg) and fentanyl (0.05 mg/kg) intraperitoneally and an acute cranial window was implanted as described above. After 30 min,

in vivo microscopy was performed using a Olympus FV1200-MPE or Olympus MPE-RS two-photon microscopy system, equipped with a femto-second pulsed Ti:Sapphire laser (Mai Tai HP-DS or Insight DeepSee, Spectra-Physics) and laser power was attenuated by acousto-optical modulators. Emission was detected with non-descanned gallium arsenide phosphide (GaAsP) detectors. To image the genetically encoded calcium indicator Twitch2b, we used a two-photon wavelength of 840 nm to simultaneously excite both mCerulean3 and cpVenusCD. Fluorescence of mCerulean3 and cpVenusCD was collected in a cyan channel (here referred to as "CFP") and yellow channel ("YFP"), respectively, using emission barrier filter pairs with 455-490 and 526-557 nm. Images were acquired in 12 bit with an 25x/1.05 dipping cone water-immersion objective, pixel size of 124 nm $pixel^{-1}$, dwell time of 2.0 µs $pixel^{-1}$ and a laser power of 30-50 mW measured in the back focal plane. Volume stacks penetrating 30-60 µm into the cortical layer I from the surface were acquired with a Z-spacing of 1 µm. For EGTA experiments, treatment solution (Ca^{2+} and Mg^{2+} free artificial cerebro-spinal fluid ± 50 mM EGTA, Sigma-Aldrich) was applied for incubation after the first imaging timepoint and used as immersion liquid during the second imaging timepoint.

Imaging of spine calcium activity was done using isoflurane anesthesia and a resonant scanner system at 15 Hz (Olympus MPE-RS) and continuous monitoring as stated above (section "*chronic in vivo* imaging of neuronal activity"). Images were acquired using a 25x/1.05 dipping cone water-immersion objective (Olympus) with a zoom of 4x and a pixel size of 249 nm $pixel^{-1}$. Fluorescence of mCerulean3 and $cpVenus^{CD}$ was collected in a cyan and yellow channel, respectively, using barrier filter pairs.

We observed no signs of photodamage in both healthy animals and c-MS animals over the imaging period using these imaging conditions. Animals showing signs of traumatic damage after window implantation were excluded from the analysis. We observed no obvious difference in the fraction of

spines with elevated calcium between the two stated methods of anaesthesia or when the dura mater was removed before imaging.

Electron microscopy

For electron microscopy, perfusion was performed on anesthetized mice with 5 mL HBSS, followed by 30 mL fixative (2.5% glutaraldehyde, 4% paraformaldehyde in phosphate buffer). Brains were extracted and further post-fixed for 8 h at 4°C in the same fixative. Afterwards, sagittal sections were done using a tissue slicer (Alto). The slice containing the cytokines (or sham) injection site were collected and further post-fixed with 2% OsO4 and 1.5% Ferocyanide (Science Services), dehydrated by ethanol then acetone and Epon-embedded (Serva). 50 nm ultrathin sections from the area corresponding to the imaging site (2-3 mm away from injection) were contrasted with 4% uranyl acetate (Science Services) and lead citrate (Sigma). The imaging was done on a TEM Jeol 1400+ (Jeol) equipped with a ruby camera (8M pixel, Jeol). The qualifications for the density of layer 1 myelin sheath was done within 60 µm from the brain surface at 4000X on 720 μm^2 areas and the synaptic density was measured at the same depth at 8000X on 185μm^2 areas.

Flow cytometry

To isolate phagocytes from brain, 4 groups of *Ccr2*^{RFP} *x BiozziABH* mice (n=3, n=3, n=10, and n=10 in healthy control, MOG immunized, c-MS day3 mice treated with vehicle, and c-MS day3 mice treated with CSF1-R inhibitors (Sanofi)) were transcardially perfused with ice-cold PBS directly after blood withdrawal and brains were isolated. Tissue was cut in small pieces and digested in RPMI containing 2% fetal calf serum (Sigma-Aldrich, 10082147), 25mM HEPES (Sigma-Aldrich, H0887), DNase I (10ng/ml, StemCell Technologies, 07900) and Collagenase D (0,8mg/ml, Roche, 11088866001) for 30 min at 37°C. Digestion was stopped by adding 1:100 dilution of 0.5M EDTA (Sigma-Aldrich) solution. After filtering the suspension through 70 µm cell strainers (Falcon, 10788201), it was resuspended in

cold Dulbecco's PBS (Sigma, D8537) and centrifuged for 5 min at 1500 r.p.m. . Supernatants were discarded and the pellet was resuspended in 25% solution of Percoll (Sigma-Aldrich, P1644). After 30 min of gradient centrifugation at 10.800 r.p.m., the myelin and red cells layers were removed and the remaining solution was filtered through 70 μm cell strainers (Falcon, 10788201). Dulbecco's PBS (Sigma, D8537) was added and the supernatant was discarded after 5 min centrifuge at 1500 r.p.m. . Stainings were performed in ice-cold PBS following LIVE/DEAD staining (1:400, Invitrogen, L34957) for 30 min and Fc-receptor blockade (CD16/32, 1:400, BD Pharmingen, 55314) for 15 min. The following antibodies were used: Alexa Fluor 700 anti-mouse CD45 (1:400, Biolegend, 103128), APC-Cy7 rat anti-CD11b (1:300, BD Pharmingen, 557657), APC anti-mouse CD40 (1:100, Biolegend, 124612), PE/Cy7 anti- mouse CD86 (1:100, Biolegend, 105014) and BV711 rat anti-mouse MHC II (I-A/I-E) (1:200, BD Horizon, 563414) incubated for 30 min. Afterwards, cells were washed and subjected to analysis. Cells were sorted on a FACSAria Fusion cell cytometer (BD Biosciences) and results were analyzed by FlowJo software.

RNA extraction, library preparation and sequencing

For RNA extraction, samples were first randomized, then total RNA was extracted using the Picopure RNA Isolation kit (Thermo Fisher). RNA quantification and quality assessment was performed using a Nanodrop 8000 and RNA Pico 6000 (Bioanalyzer), respectively. Total RNA was diluted to 1 ng/ 10 μl of water prior to Oligo(dT) priming from Takara's SmartSeq v4 Ultra Low Input RNA kit. Enriched mRNA was converted to full-length cDNA then amplified using 11 PCR cycles (17 cycles for very low input samples). Final sequencing libraries were prepared and uniquely indexed using Illumina's Nextera XT kit without modification to the standard protocol. Integrity of each sample library was assessed using the DNA High Sensitivity kit and run on a Bioanalyzer 2100. Library quantification was performed using Qubit then diluted to 1nM and pooled together. To prepare for sequencing, pooled libraries were denatured with NaOH then diluted to 1.8 pM according to Illumina's denaturation protocol for a

NextSeq500. Sequence runs were performed on an Illumina NextSeq500 using the High output kit and a 2x76bp paired end run.

CSF1/LPS stimulation and phagocytosis assays

Primary murine microglia were isolated with immunopanning and plated at 50k/well in PDL-coated 96-well plates and rested overnight. For the stimulation assay, cells were treated with CSF1-R inhibitor (100nM, Sanofi) for 24 hours. CSF1 (100ng/mL) or LPS (10ng/mL) was then added for an additional 24 hours and culture supernatants were collected and assayed for MCP-1 (CCL2) or IL-12p40 with ELISA. For phagocytosis assay, cells were treated with vehicle (DMSO) or CSF1-R inhibitor (100 nM and 500 nM, respectively, Sanofi) for 30 minutes at 37°C, 5% CO2. Cells were then stimulated with CSF1 (100 ng/mL) for 30 minutes. Human synaptoneurosomes were prepared using the following protocol: 36.22 µL crude synaptoneurosomes were generated and combined with 63.78 µL 0.1M sodium bicarbonate and 1 µL pHrodo Red (Invitrogen). The synaptoneurosome mixture was incubated at room temperature for 45 minutes in the dark. The mixture was then washed with PBS twice and finally re-suspended in 200 µL media. This labeled synaptoneurosome stock was then diluted in media (100 µL stock in 8 mL media) and 100 µL added to each well. Plates were then imaged in the Incu-Cyte Live Imaging System (Sartorius) for 8 hours, measuring red object counts in primary murine microglia cells. The experiment was repeated in n =3 litters with n=4 wells per group.

Quantification and Statistical Analysis

Histopathological analysis

To evaluate CD3 and Mac-3 positive cells an image was chosen at the distance of 1700 to 2000 µm from the midline on both hemispheres using Pannoramic viewer software (3D-Histech) and rotated using Irfanview software. Images were imported in ImageJ software [73] , cortical layers I, II-IV and V were determined and cell counter plugin was used to evaluate each layer. For Bielschowsky's staining, 2

parallel lines with a distance of 150 µm were located on each images sampled from the abovementioned area and the crossing filaments from each line was counted to evaluate axon density. For quantification of the density of CD4 and CD8 positive cells a region of interest was selected on each hemisphere at the distance of 1000 to 2000 µm from the midline and the cells were counted using cell counter plugin. In the same region, c-Fos and c-Jun positive cells were evaluated as a percentage of counterstained cells. MBP areas were quantified applying a custom rule-set in Definiens Developer XD (Definiens AG, Version 2.7.0). Cortical regions were first manually selected and regions were rotated so that the cortical layers were horizontally oriented. Tissue was detected and cortical layers were automatically defined by their distance to the tissue-background border. Color deconvolution was applied to separate DAB and counterstain. MBP signals in the DAB channel were considered positive if above a defined intensity threshold. Total DAB+ area was reported for each region individually.

Confocal image processing and analysis

Post-processing of presented confocal images was done using the open-source image analysis software ImageJ [73] and Photoshop (Adobe). Further image processing steps are stated in the text or figure legends.

Reconstruction of cortical pyramidal neurons

Confocal images used for analyzing spine density were deconvoluted with Huygens Essential version 16.05 (Scientific Volume Imaging, The Netherlands, http://svi.nl) using maximum 70 iterations and the classical MLE algorithm. Cortical pyramidal neurons were reconstructed using Volume Integration and Alignment System (VIAS) software [74]. Semi-automatic tracing of the apical dendrite and spines was performed by NeuronStudio software [74,75]. For analyzing spine density over time and evaluating the therapeutic effects of CSF1-R inhibitor compound, dendritic stretches located at the layers III to IV with a dendritic radius of 0.55 to 1 µm coming from pyramidal layer V neurons were chosen.

Neurons were located 1000 to 2000 µm from the midline, contralateral to the injection site and in a distance of maximum 600 µm caudal to the injection. Default classification of spine types by Neuronstudio software (mushroom, stubby and thin) in automatically detected spines showed reduction of all spine types in c-MS mice at d3 compared to healthy controls (n=62 and n=48 dendritic stretches from each group, respectively; percentage of each spine type to normalized healthy control: mushroom: 62.77±3.43 %; thin: 80.92±5.70 %; and stubby: 76.42±5.26 %; mean±SEM; two-way ANOVA followed by Bonferroni's multiple comparisons test reveals significant reduction vs. healthy control for mushroom spines ($p<0.001$), thin spines ($p<0.05$) and stubby spines ($p<0.01$).

Analysis of excitatory and inhibitory synapse density

Three images within layers III-IV located at 1000 to 2000 µm from the midline were acquired from each hemisphere of coronal brain sections at a distance of 270 µm caudal to the injection site or a similar area in the healthy controls. Synaptic contacts were analyzed using a custom algorithm in cognition Network Language (Definiens Developer XD software, Version 2.7.0, Munich, Germany). First, nuclei were excluded from the area to analyze based on DAPI signal. Synaptic markers were counted as positive, if they were at least 20% brighter than the tissue background in the corresponding color channel. Objects smaller than 16 pixel^2 were excluded. Remaining objects were split based on intensity using a watershed algorithm and their shapes stored as a binary image. To quantify putative synaptic contacts each synaptic structure was first reduced to its center of gravity to create non-overlapping points. These points were then again grown into their respective signals based on the binary images until touching a neighbouring image object. For each object, the number of contacts to neighboring objects was quantified. Data was summarized with R (R-project, version 3.6.1; R Core Team (2014). R: A language and environment for statistical computing. R Foundation for Statistical Computing, Vienna, Austria. URL https://www.R-project.org/). Synaptic contacts per µm^2 were averaged over six images per animal for each staining and reported. Ratio of excitatory to inhibitory synapses were calculated per animal.

Phagocyte infiltration and activation

Overview images were segmented in cortical layers using a nucleic acid stain (NeuroTrace) and analyzed in ROIs 1000-2000 µm laterally to the midline. In the MHC II channel, five ROIs were located in the background area and the mean and the standard deviation (SD) of the intensity was determined in each image. Signals above the mean+3SD of the background intensity were considered as positive for MHC II. Numbers of $CX_3CR\text{-}1^{GFP}$ cells, co-labelling of $CX_3CR\text{-}1^{GFP}$ and MHC II immunofluorescence and numbers of $Ccr2^{RFP}$ cells or Iba-1 ^{positive}, $CX_3CR\text{-}1^{GFP}$ negative cells were analyzed using the cell counter plugin (ImageJ) and reported per volume. Microglial activation is presented as % of MHC II positivity of all $CX_3CR\text{-}1^{GFP}$ cells. For accessing the effect of CSF1-R inhibitor compound, three counting frames (200 x 200 µm) per section (six sections per animal) were chosen in layers III-IV at 1000 to 2000 µm contralateral to the cytokine injection. For generating the heatmap of inflammation, cells were evaluated in counting frames of 500 x 500 µm size.

Analysis of synapse phagocytosis

At least ten individual $CX_3CR\text{-}1^{GFP}$ or $Ccr2^{RFP}$ cells per animal were reconstructed automatically by Imaris software (BitPlane, South Windsor, CT, USA) in a stack of 5.14 µm. The rendered surface was used as a mask on Synapsin-1, PSD95, Homer-1 channels and the spot function was used to identify the positive signals (spheres). Average intensity of five ROIs in the non-positive background were used to define the threshold in each channel for visual confirmation of spheres. Spheres that were not fully engulfed by the phagocytic cell or not visually confirmed were manually removed. Spheres were assessed on the LAMP1 channel to evaluate colocalization. The LAMP1 channel was further masked by the cell surface and the volume was automatically reconstructed to identify the LAMP1 volume per cell. In the $CX_3CR\text{-}1^{GFP}$ cells delta (Δ) refers to subtraction of average volume of healthy controls from vehicle or CSF1-R treated c-MS mice.

Analysis of neuronal activity

The analysis of neuronal activity recordings was performed with a custom software/graphical user interface. The software aligns the single frames of the data sets using a cumulative correlation maximization algorithm with the mRuby signal as reference. Using a calculated reference image (average frame, denoised running average, channel difference, coefficient of variation, between others) the software allows ROI definition manually or semi- automatically, providing an unique ID for each neuron. The ROIs defined at previous timepoints were imported into new recordings and automatically adjusted to compensate for the possible minor morphological changes. The pixels inside each ROI were averaged to extract a time signal of each neuron. The baseline signal F_0 was calculated as the 10-percentile of the time series in a rolling window of 6 seconds. Signal was calculated using the following formula: $dFF = (F-F_0)/F_0$, which if necessary was corrected for neuropil contamination by subtracting a fraction (usually 60%) of the dFF calculated using a background ROI surrounding the neuron and excluding any other marked cell. The final dFF was processed with an exponential filter with a time constant of (0,01). Calcium events for the recording of each neuron were calculated using a non-negative deconvolution algorithm [76], where the resulting likelihood per frame is processed to separate the individual events by summation and thresholding. The final neuronal activity for each neuron was calculated from the average of 3 recordings (see *in vivo* imaging section).

Neuronal population correlation analysis

The longitudinal comparison of the neuronal activity to baseline levels was performed on neurons with an activity superior or equal to 0.5 calcium event per minute on average from the baseline measurements. The distribution depicted in the violin plots was obtained by calculating the change in activity for every measured neuron by dividing the average activity at 3 or 17 days post injection (sham or cytokines in the c-MS model) with the corresponding baseline activity. The binned neuronal activity

comparison from baseline to final timepoint was measured for every animal in both sham-injected and cortical MS groups.

In order to assess the signal correlation for every neuron at each timepoint, every region was imaged for three sessions (5 minutes/session), and a signal correlation matrix was obtained for each session. The correlation similarity between any two such matrices is defined as the correlation of the individual entries in the upper-triangular part of the correlation matrices [13]. To compare the population dynamics at any given timepoint to the initial population dynamics, the similarity between all correlation matrices at the given timepoint and all correlation matrices in the initial session were calculated and the resulting values averaged. For the c-MS d3, c-MS d10 and c-MS d17 timepoints this involves averaging nine similarities (the three signal correlation matrices at each timepoint compared to the three initial signal correlation matrices). For the initial session, this similarity involved three comparisons.

In order to investigate the hypothesis that the c-MS data and the sham data may differ at an intermediate timepoint (day 3 or 10) but recover by day 17, we fit the timecourse data for each mouse with a cubic polynomial. This the simplest polynomial that can allow for the shapes we observed: both a monotonic decrease over the four timepoints and a decrease followed by an increase. The experimental data gave us 7 polynomials (7 areas from 4 animals) that were averaged (orange curve in **Fig 3e**). In order to generate a null distribution for the average of such polynomials from the sham condition, we selected 5 out of the 10 sham experiments (10 areas from 4 animals), and averaged their polynomials to generate one data point in this null distribution. We repeated this for all 252 subsets of 5 choices from the 10 sham experiments to obtain an approximation for the null distribution. We chose to take samples of 5 out of 10 because this generates the most number of samples and allows us to approximate the null distribution accurately. The null distribution is shown in black in **Fig 3e**: the median is shown in thick solid black, the 5-th and 95-th percentiles are shown in dotted black and the maximum and minimum

values are shown in thin solid black. This analysis revealed that at day 3, and only at day 3, the red experimental line is outside the null distribution. This was confirmed by performing an *a posteriori* Mann-Whitney test for the difference of the distributions at day 3 (p-value=0.035). The software Matlab (R2018b) was used to perform the correlation and polynomial analysis.

Dendritic and spine calcium levels

For analysis of Ca^{2+} levels in spines and dendrites using the Twitch2b sensor signal, the CFP and YFP (FRET) channels were individually visualized in a greyscale look-up table to determine the region of interest. Fluorescence intensities of the spine head or 5 regions in the dendrites shaft were measured in the CFP and YFP channels, respectively, and nearby non-neurite areas were selected for background correction. As we detected crosstalk from the CFP to the YFP channel (not vice-versa), we corrected the YFP signal by subtracting the measured crosstalk-fraction of the CFP signal. Background-corrected YFP/CFP ratios were interpreted as a proxy of Ca^{2+} concentration as previously established for the used FRET-based calcium sensor. We excluded spines that exhibited a signal-to-noise ratio < 5.2, as measured in YFP channel. Spines or dendrites were considered to be Ca^{2+}-elevated/high if YFP/CFP ratios showed elevation greater than mean plus 3 standard deviations of the ratios measured in healthy control animals. When datasets measured at two different microscope systems were plotted together, data was normalized to the respective control mean measured on each system. Population analysis of spine and dendritic Ca^{2+} and analysis of CSF1-R inhibitor treatment experiments was performed by an investigator blinded to the treatment status. For dynamic analysis of spine fate with and without EGTA application, per region 10 dendrites including all spines were identified in both timepoints (t_1 =0 h and t_2 = 2 h) and measured. To confirm stability of net loss rates, a third imaging timepoint (4 h) was evaluated for a subgroup of animals, showing a net loss rate of 20 % for high Ca^{2+} spines between 2 and 4 hours of imaging (n = 4 c MS mice) as compared to 27 % between 0 and 2 hours of imaging (see **Figure 4g**). Data was stratified

and grouped according to Ca^{2+} decrease ($[Ca^{2+}_{t2}] < ([Ca^{2+}_{t1}])$, Ca^{2+} increase ($[Ca^{2+}_{t2}] > 2 \times [Ca^{2+}_{t1}]$), spine loss (not detectable in t2) using a custom R script.

For the assessment of spine calcium activity, resonant scanner-derived images were acquired (see *In vivo* imaging section) and registered using a custom Matlab script. Spine and nearby non-neurite background ROIs were manually defined and measured over time in the CFP and YFP channels as stated above. Background-corrected YFP/CFP ratios were interpreted as a proxy of Ca^{2+} concentration. Raw values were smoothed by removing single outlier values (negative, >15) and using a 3-neighboring average algorithm. Baseline drift was assessed using a 10s moving average and, when no drift was observed, overall baseline mean and standard deviation calculated. Spiking activity was defined as above-threshold activity (baseline mean plus 2 SD) for > 0.25s and calculated as frequency (min^{-1}).

Ratiometric images presented in this work were processed as follows: in ImageJ, intensity projections of 3D stack sections were created from CFP and YFP images individually and a binary thresholded mask of dendritic outlines was generated from the image channel with higher signal-to-noise (after application of pixel outlier filters). Projection images were each multiplied by the binary mask and the resulting images divided by each other (YFP/CFP). The resulting image was pseudo-colored with a custom look-up table spanning from blue (low Ca^{2+}) via red to yellow (high Ca^{2+}) hues. Images were exported as RGB images to Photoshop, greyscale images were additionally despeckled.

RNA sequence data analysis

Data analysis was completed using Omicsoft Array Studio. On average, each sample was sequenced at a depth of 52 million paired-end reads. Illumina adaptors were stripped during the BCL to FastQ conversion. All raw data was QC'd using the "Raw Data QC" function within Array Studio. Poor quality reads were filtered out using a Q score cutoff of 20. Following the above filter criteria, about 41 million paired-end reads per sample were uniquely mapped to the B38 Mouse Reference Genome using the

Ensembl.R90 Gene Model. Raw counts were then converted to FPKM using the "Report Gene/Transcript Counts" function in Array Studio. FPKM was filtered using a cutoff of 0.1 then normalized using the 75th quantile. A constant of 1 was added to all normalized FPKM data prior to a Log2 transformation. This data was used in all downstream analysis including Principal Component Analysis (PCA), heatmaps, t-tests and pathway analysis (Ingenuity). Outliers (a total of nine) were confirmed visually using PCA plots as well as Hierarchical Clustering (unsupervised). t-tests were generated using the General Linear model in Array Studio. Pathway analysis was completed using fold change and p-values obtained via TTests and imported into Ingenuity (Qiagen).

snRNA-seq data analysis

Raw single-nucleus RNA-sequencing data from multiple sclerosis and control brains acquired by Schirmer and colleagues was obtained from the NCBI Sequence Read Archive (SRA) under the accession number PRJNA544731 [70] . In this analysis a total of 48,919 single-nucleus profiles derived from snap-frozen brain tissue sections encompassing the cortical gray matter with attached meninges and underlying subcortical white matter (12 tissue blocks from 10 progressive MS patients and 9 tissue blocks from 9 controls patients) were analysed as described in more detail in Schirmer et al.[70] . The expression matrix containing the UMI per gene reads in each nucleus was obtained by demultiplexing the raw data with Cell Ranger software (10x Genomics, Pleaston, USA). Data clean-up, filtering, transformation and scaling, dimensional reduction, clustering and differential gene expression analysis was done using the Seurat package [77] in R (R-project, version 4.0.2; R Core Team (2020). R: A language and environment for statistical computing. R Foundation for Statistical Computing, Vienna, Austria. URL https://www.R-project.org/). Filtering thresholds were adjusted according to Schirmer et al. [70] . After t-Stochastic neighbor embedding (t-SNE) and subsequent cluster analysis, the distribution of the expression levels of CSF1R, CSF1 and IL34 were analyzed. To map CNS cell types to the clusters, the expression levels of the following marker genes were assessed (according to Schirmer et al. [70] : P2RY12 (microglia), AQP4

(astrocytes), PLP1 (oligodendrocytes), SLC17A7 (excitatory neurons) and GAD2 (inhibitory neurons). Clusters of cells expressing the respective marker genes were subjected to further analysis. Cluster 23 was comprised of cells expressing both P2RY12 and PLP1 and, was therefore, excluded from further analysis. Likewise, cluster 28 was excluded from further analysis since it exclusively encompassed cells derived from MS samples.

Statistical analysis

Sample sizes were chosen according to previous *in vivo* imaging studies [30]. Statistical significance was calculated with Prism (Versions 6.0 and 7.0, Graphpad) using ANOVA and t-tests (where normal distribution could be assumed) or Kruskal-Wallis and Mann-Whitney U test (where non-normal distribution was suspected and confirmed by Shapiro-Wilk test) as described in the figure legends. Data are expressed as the mean ± standard error of the mean. Obtained p-values were corrected for multiple comparisons and stated as significance levels in the figure legends. In all analyses $p<0.05$ was considered statistically significant.

Data and code availability

All data is available in the manuscript or the supplementary materials. Raw data is available upon reasonable request to the corresponding author. The codes used to perform the cross correlation analysis and the codes of the graphical user interface used to analyze the calcium events are publicaly available on the github repository: https://github.com/portugueslab/Jafari-et-al-2020. The codes used to reanalyze the snRNA-seq data from Schirmer et al. are publicaly available on the github repository: https://github.com/engelsdaniel/schirmer_reanalyzed .

References

72. Holtmaat, A. et al. Long-term, high-resolution imaging in the mouse neocortex through a chronic cranial window. *Nat. Protoc.* **4**, 1128–1144 (2009).

73. Schneider, C. A., Rasband, W. S. & Eliceiri, K. W. NIH Image to ImageJ: 25 years of image analysis. *Nat. Methods* **9**, 671–675 (2012).

74. Rodriguez, A. et al. Automated reconstruction of three-dimensional neuronal morphology from laser scanning microscopy images. *Methods* **30**, 94–105 (2003).

75. Wearne, S. L. et al. New techniques for imaging, digitization and analysis of three-dimensional neural morphology on multiple scales. *Neuroscience* **136**, 661–680 (2005).

76. Vogelstein, J. T. et al. Fast nonnegative deconvolution for spike train inference from population calcium imaging. *J. Neurophysiol.* **104**, 3691–3704 (2010).

77. Butler, A., Hoffman, P., Smibert, P., Papalexi, E. & Satija, R. Integrating single-cell transcriptomic data across different conditions, technologies, and species. *Nat. Biotechnol.* **36**, 411–420 (2018).

SUPPLEMENTARY INFORMATION

Supplementary Figures 1-12

Supplementary Movie 1.

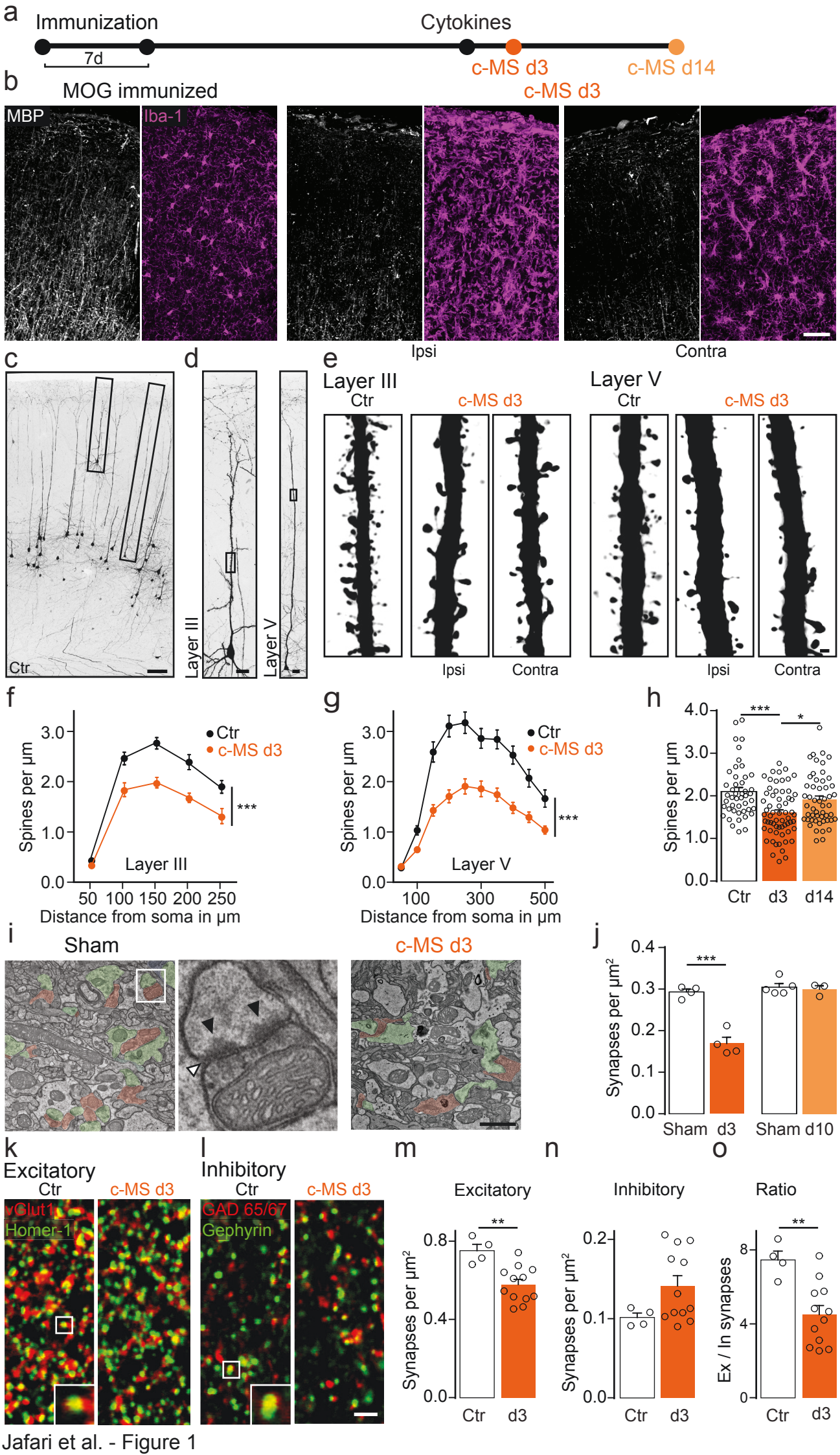

Jafari et al. - Figure 1

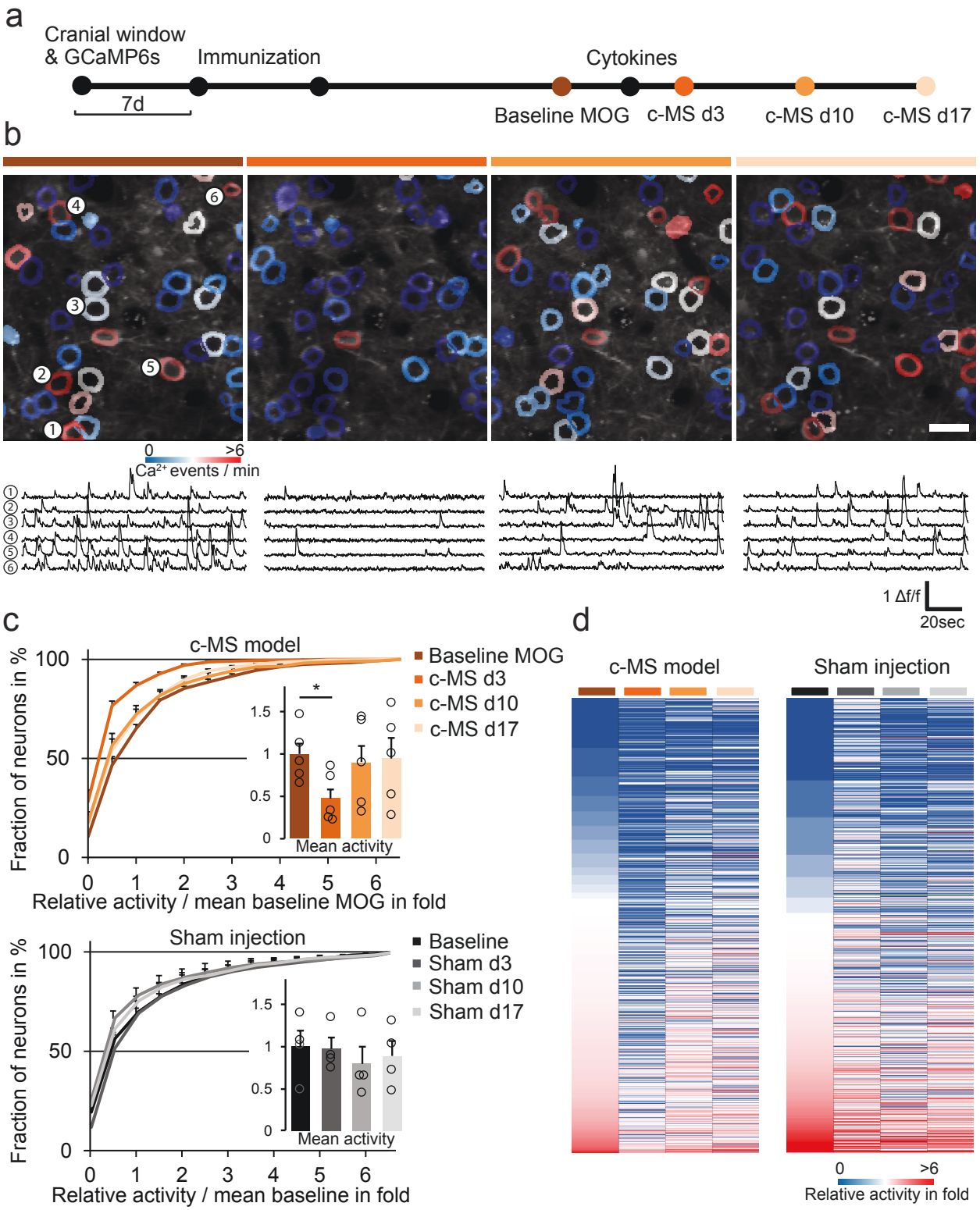
a
Cranial window
& GCaMP6s
Immunization
Cytokines
7d
Baseline MOG
c-MS d3
c-MS d10
c-MS d17
b
0
>6
Ca2+ events / min
1 Δf/f
20sec
c
c-MS model
Baseline MOG
c-MS d3
c-MS d10
c-MS d17
Fraction of neurons in %
Relative activity / mean baseline MOG in fold
Mean activity
Sham injection
Baseline
Sham d3
Sham d10
Sham d17
Relative activity / mean baseline in fold
d
c-MS model
Sham injection
Relative activity in fold

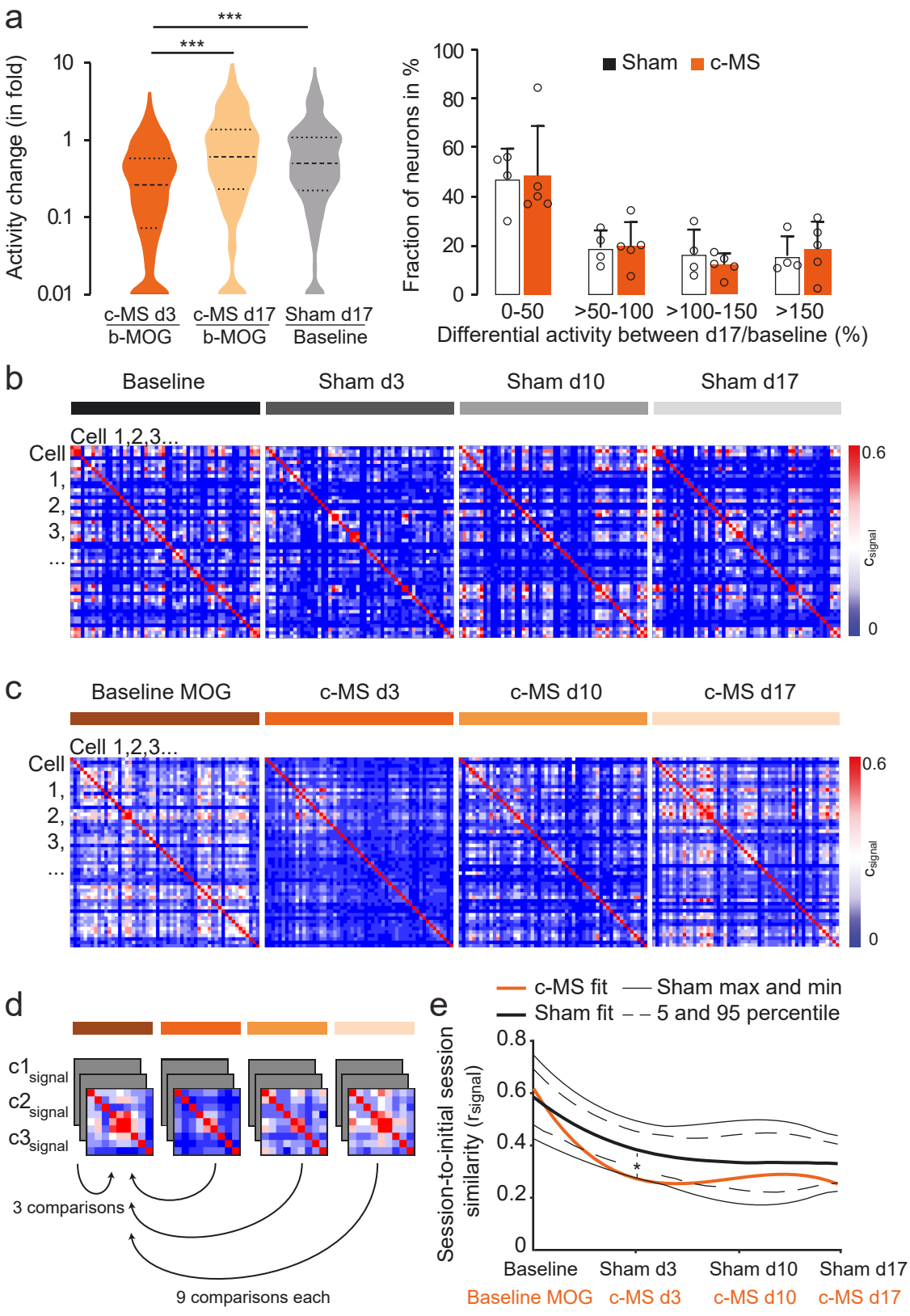
a
***
***
Activity change (in fold)
10
1
0.1
0.01
c-MS d3 / b-MOG
c-MS d17 / b-MOG
Sham d17 / Baseline
Fraction of neurons in %
100
80
60
40
20
0
Sham
c-MS
0-50
>50-100
>100-150
>150
Differential activity between d17/baseline (%)
b
Baseline
Sham d3
Sham d10
Sham d17
Cell 1,2,3...
Cell 1, 2, 3, ...
0.6
csignal
0
c
Baseline MOG
c-MS d3
c-MS d10
c-MS d17
Cell 1,2,3...
Cell 1, 2, 3, ...
0.6
csignal
0
d
c1signal
c2signal
c3signal
3 comparisons
9 comparisons each
e
c-MS fit
Sham fit
Sham max and min
5 and 95 percentile
Session-to-initial session similarity (rsignal)
0.8
0.6
0.4
0.2
0
*
Baseline
Sham d3
Sham d10
Sham d17
Baseline MOG
c-MS d3
c-MS d10
c-MS d17

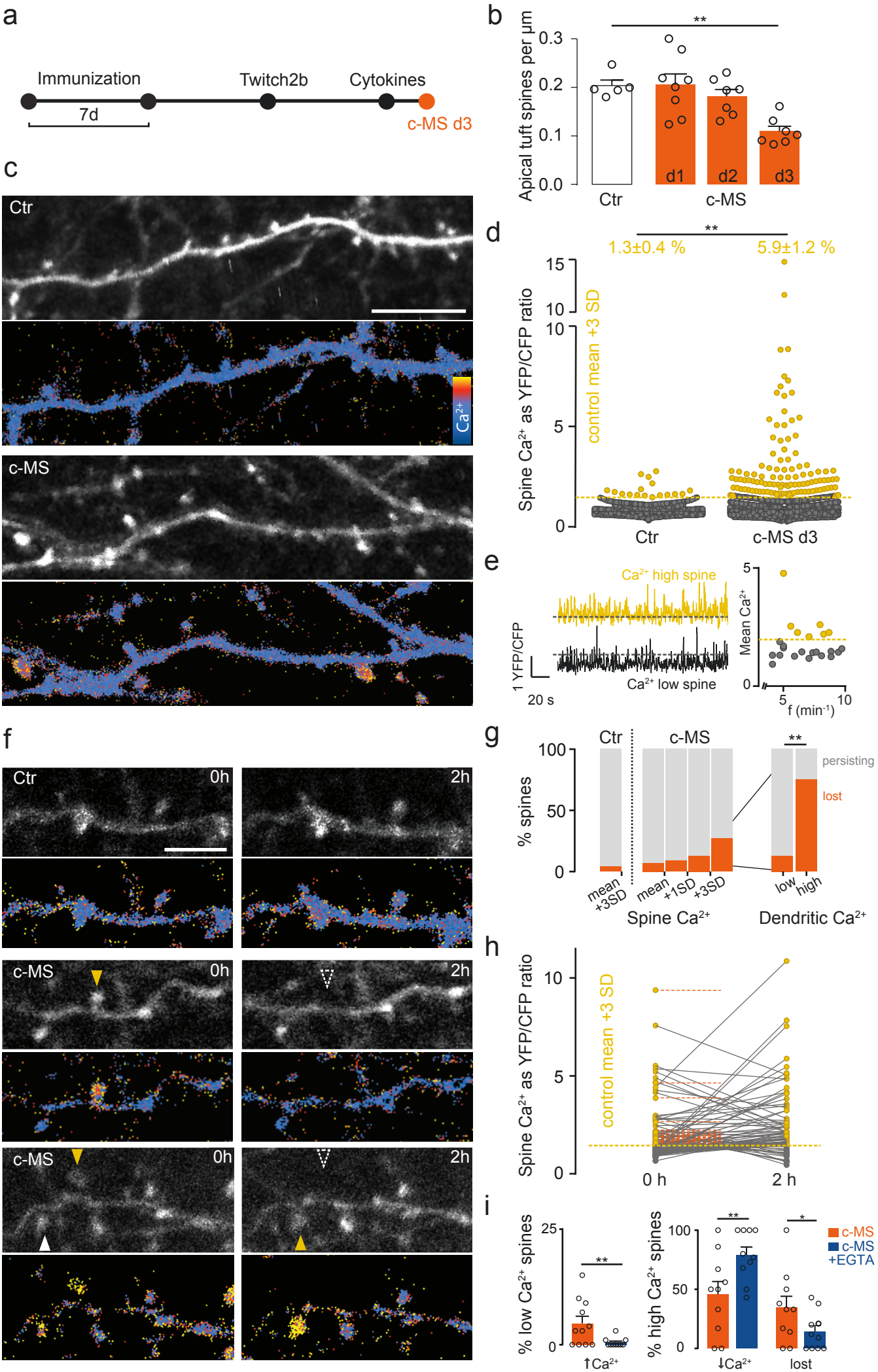
a
Immunization
7d
Twitch2b
Cytokines
c-MS d3
b
Apical tuft spines per µm
0.3
0.2
0.1
0.0
**
Ctr
c-MS
d1
d2
d3
c
Ctr
Ca2+
c-MS
d
**
1.3±0.4 %
5.9±1.2 %
Spine Ca2+ as YFP/CFP ratio
control mean +3 SD
15
10
5
0
Ctr
c-MS d3
e
Ca2+ high spine
Ca2+ low spine
1 YFP/CFP
20 s
Mean Ca2+
f (min-1)
f
Ctr
0h
2h
c-MS
g
Ctr
c-MS
**
persisting
lost
% spines
100
50
0
mean +3SD
mean +1SD
+3SD
low
high
Spine Ca2+
Dendritic Ca2+
h
Spine Ca2+ as YFP/CFP ratio
control mean +3 SD
10
5
0
0 h
2 h
i
% low Ca2+ spines
25
0
**
↑Ca2+
% high Ca2+ spines
100
50
0
**
*
↓Ca2+
lost
c-MS
c-MS +EGTA

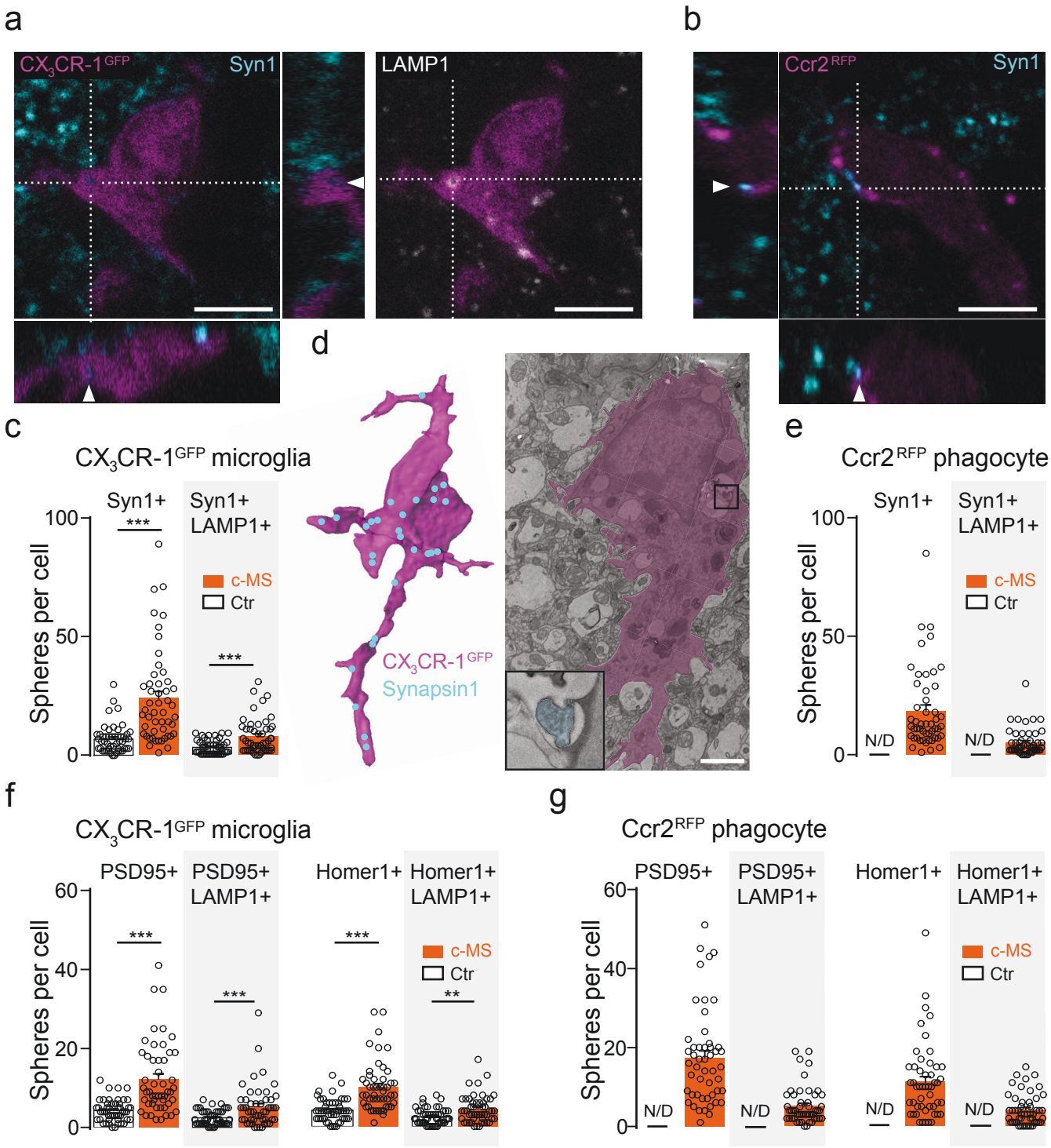
a
CX3CR-1GFP
Syn1
LAMP1
b
Ccr2RFP
Syn1
d
CX3CR-1GFP
Synapsin1
c
CX3CR-1GFP microglia
Syn1+
Syn1+ LAMP1+
Spheres per cell
100
50
0
***
***
c-MS
Ctr
e
Ccr2RFP phagocyte
Syn1+
Syn1+ LAMP1+
N/D
N/D
f
CX3CR-1GFP microglia
PSD95+
PSD95+ LAMP1+
Homer1+
Homer1+ LAMP1+
60
40
20
0
**
g
Ccr2RFP phagocyte

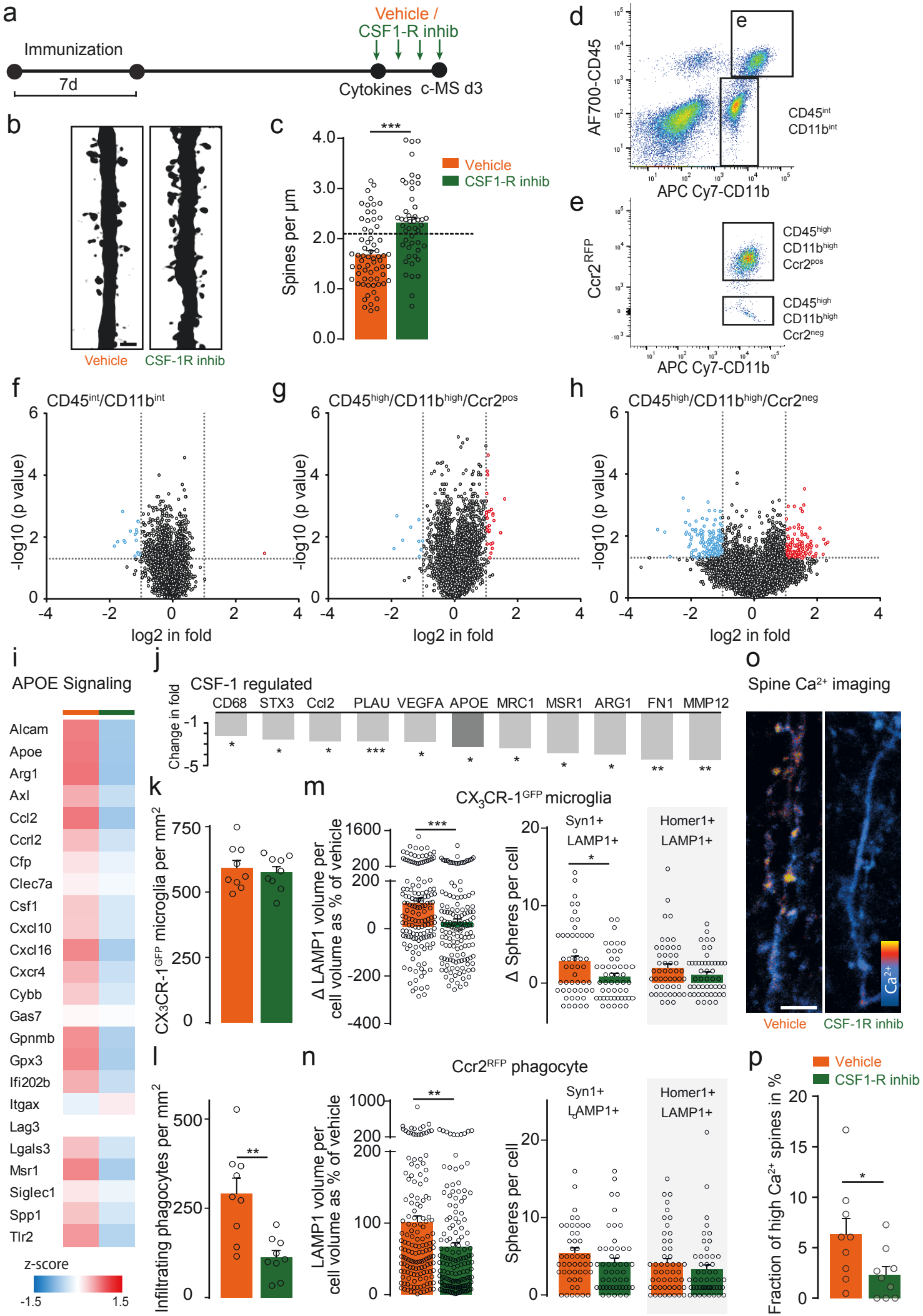
a
Immunization
7d
Vehicle / CSF1-R inhib
Cytokines
c-MS d3
b
Vehicle
CSF-1R inhib
c
Spines per µm
Vehicle
CSF1-R inhib
d
AF700-CD45
APC Cy7-CD11b
CD45int CD11bint
e
Ccr2RFP
CD45high CD11bhigh Ccr2pos
CD45high CD11bhigh Ccr2neg
f
CD45int/CD11bint
g
CD45high/CD11bhigh/Ccr2pos
h
CD45high/CD11bhigh/Ccr2neg
-log10 (p value)
log2 in fold
i
APOE Signaling
Alcam
Apoe
Arg1
Axl
Ccl2
Ccrl2
Cfp
Clec7a
Csf1
Cxcl10
Cxcl16
Cxcr4
Cybb
Gas7
Gpnmb
Gpx3
Ifi202b
Itgax
Lag3
Lgals3
Msr1
Siglec1
Spp1
Tlr2
z-score
-1.5
1.5
j
CSF-1 regulated
Change in fold
CD68 STX3 Ccl2 PLAU VEGFA APOE MRC1 MSR1 ARG1 FN1 MMP12
k
CX3CR-1GFP microglia per mm2
m
CX3CR-1GFP microglia
Δ LAMP1 volume per cell volume as % of vehicle
Δ Spheres per cell
Syn1+ LAMP1+
Homer1+ LAMP1+
l
Infiltrating phagocytes per mm2
n
Ccr2RFP phagocyte
LAMP1 volume per cell volume as % of vehicle
Spheres per cell
o
Spine Ca2+ imaging
Ca2+
Vehicle
CSF-1R inhib
p
Vehicle
CSF1-R inhib
Fraction of high Ca2+ spines in %

Supplementary Information for

Local calcium accumulations promote phagocyte-mediated synapse removal in cortical neuroinflammation

Mehrnoosh Jafari [1,2]†, Adrian-Minh Schumacher[1,2]†, Nicolas Snaidero[1,3,4]†, Emily M. Ullrich Gavilanes[1,2], Tradite Neziraj[1,2], Virág Kocsis-Jutka[1,2], Daniel Engels[1,2], Tanja Jürgens[5], Ingrid Wagner[5,] Juan Daniel Flórez Weidinger[6,7,8,9], Stephanie S. Schmidt[1], Eduardo Beltrán[1,2], Nellwyn Hagan[10], Lisa Woodworth[10], Dimitry Ofengeim[10], Joseph Gans[11], Fred Wolf[6,7,8,9], Mario Kreutzfeldt[5,12], Ruben Portugues[13,14], Doron Merkler[5,12]*#, Thomas Misgeld[3,4,14]*# and Martin Kerschensteiner[1,2,14]*#

[1] Institute of Clinical Neuroimmunology, University Hospital, Ludwig-Maximilians Universität München, Munich, Germany

[2] Biomedical Center (BMC), Faculty of Medicine, Ludwig-Maximilians Universität München, Martinsried, Germany

[3] Institute of Neuronal Cell Biology, Technische Universität München, Munich, Germany

[4] German Center for Neurodegenerative Diseases (DZNE), Munich, Germany

[5] Department of Pathology and Immunology, University of Geneva, Geneva, Switzerland

[6] Theoretical Neurophysics, Max Planck Institute for Dynamics and Self-Organization, Göttingen, Germany

[7] Bernstein Center for Computational Neuroscience, University of Göttingen, Göttingen, Germany

[8] Max Planck Institute for Experimental Medicine, Göttingen, Germany.

[9] Center for Biostructural Imaging of Neurodegeneration, Göttingen, Germany.

[10] Sanofi Neuroscience, Framingham, MA, USA

[11] Translational Sciences Genomics, Sanofi, Framingham, MA, USA

[12] Division of Clinical Pathology, Geneva University Hospital, Geneva, Switzerland

[13] Sensorimotor Control, Max Planck Institute of Neurobiology, Martinsried, Germany

[14] Munich Cluster for Systems Neurology (SyNergy), Munich, Germany

† These authors contributed equally to this work.

[#] Co-senior authors

*Correspondence to:

M.K. (martin.kerschensteiner@med.uni-muenchen.de)

D.M. (doron.merkler@unige.ch)

T.M. (thomas.misgeld@tum.de)

This PDF file includes:

Supplementary Figure 1-12
Captions for Supplementary Movie S1

Other Supplementary Materials for this manuscript include the following:

Movie S1

Supplementary Figure 1 - Histopathological and clinical characterization of a mouse model of cortical multiple sclerosis.

(**a**) EAE score of the c-MS d3 (n=8) and c-MS d14 mice (n=9) used in **Fig 1h**. Black dots represent EAE scores before and orange dots EAE scores after cytokine injection (n=17 mice from immunization to c-MS d3 timepoint and n=9 mice plotted until c-MS d14 perfusion time point; mean ± SEM). (**b**) Cortical spine density on d3 post cytokine injection does not show an obvious correlation with EAE score on d3 (n=114 dendritic stretches from n=17 mice; r=0.13, p=0.16; data derived from **Fig1 h**). (**c**) Spine density on d3 post cytokine injection does not correlate with average EAE score during the experiment (n=114 dendritic stretches from n=17 mice; r=0.12, p=0.21; data derived from **Fig1 h).** (**d**) Schematic of the experimental design to study histopathological changes in the cortex of age-matched control (Ctr; black), MOG immunized (brown), only cytokine injected (violet) and cortical MS model (c-MS d3, orange) mice. (**e**) Bielschowsky's staining was used to analyze axonal density in each layer. Representative images depict Bielschowsky's staining in layer I of Ctr and c-MS d3 mice (**left, middle,** respectively), axonal density was normalized to average density of the Ctr group (**right**). (**f**) MBP staining was used to analyze myelin density in each layer. Representative images depict MBP staining in layer I of Ctr and c-MS d3 mice (**left, middle,** respectively), MBP density was normalized to average density of the Ctr group (**right**). (**g**) CD3 staining was used to analyze T cells density in each layer. Representative images depict CD3 staining in layer I of Ctr and c-MS d3 mice (**left, middle,** respectively), $CD3^+$ cell density (**right**). (**h**) Mac-3 staining was used to analyze mononuclear phagocytes density in each layer. Representative images depict Mac-3 staining in layer I of Ctr and c-MS d3 mice (**left, middle,** respectively), Mac-3^+ cell density (**right**). Data shown as mean ± SEM; (n= 5, 5, 6 and 6 mice in each group). Scale bars in **e,** 15 µm; **f**, 45 µm **g** and **h,** 25 µm. Two-way RM ANOVA followed by Bonferroni's multiple comparisons test has been performed in **e-h**. *** P<0.001, **P<0.01, *P<0.05.

Supplementary Figure 2 – Cortical spine loss in c-MS mice compared to mice immunized only with MOG or injected only with cytokines.

(a) Spine density along the apical dendrite of layer V pyramidal neurons in healthy control (Ctr) mice and MOG immunized animals without cytokine injection (n=21 neurons from n=7 and 8 mice in each group, respectively; mean ± SEM). (**b**) Spine density along the apical dendrite of layer V pyramidal neurons in healthy control mice and non-immunized mice 3d after cytokine injection analysed ipsi- and contralateral to the injection site (n=21, 8 and 13 neurons from n=7 and 10 mice in each group, respectively; mean ± SEM). (**c**) Spine density along the apical dendrite of layer V pyramidal neurons in healthy control and c-MS d3 animals analysed ipsi- and contralateral to the injection site (n=21, 17 and 11 neurons from n=7 and 8 mice in each group, respectively; mean ± SEM; data derived from **Fig1 g**). Two-way RM ANOVA followed by Bonferroni's multiple comparisons test has been performed in **a-c**. *** $P<0.001$. The same Ctr group replotted in all three graphs.

Supplementary Figure 3 – Layer V projection neurons are silenced in a model of cortical multiple sclerosis.

(**a**) Scheme of the experimental timeline to study longitudinal activity in apical dendrites of layer V projection neurons in the cortical MS model (c-MS) by *in vivo* imaging of *Thy1-GCaMP6f* x *BiozziABH* mice. (**b**) *In vivo* multiphoton image of layer V apical dendrites over the course of c-MS through a cranial window; **left,** before cytokine injection (baseline MOG) and **right** 3 days (c-MS d3) post cytokine injection. **Top**: Merged GCaMP6f and autofluorescence channels allow the identification of apical dendrites (green only). **Middle**: GCaMP6f channel masked and color-coded for cytoplasmic Ca^{2+} events per minute. **Bottom**: Representative calcium activity traces displayed as delta f/f for the four apical dendrites marked in the middle panel. (**c**) Cumulative plots representing activity for the entire population of apical dendrites for each selected time point over the course of the cortical MS model. **Insets**: Mean activity normalized to baseline for MOG shown as mean ± SEM (n=3 c-MS mice, Shapiro-Wilk and paired t-test). (**d**) Heat map representation of ranked activities for single dendrites between baseline MOG and c-MS d3. (**e**) Spine density of dendritic stretches of pyramidal layer V neurons from c-MS d3 mice used in **b-d** (imaged area was used for quantification) and control mice (n=30 and n=40 dendritic stretches from n=3 and n=4 mice, respectively; mean ± SEM, unpaired t-test). Scale bar in **b**, 20µm. **P < 0.01, *P<0.05.

Supplementary Figure 4 - Recording the activity of single cortical neurons over time in the cytokine-injected gray matter.

(**a**) **Top:** Schematic of experimental design for longitudinal *in vivo* imaging of Ca^{2+} transients in layer II/III somatosensory neurons upon injection of cytokines in healthy animals, using the GCaMP6s Ca^{2+} indicator delivered via viral gene transfer (AAV1.hSyn1.mRuby2.GCaMP6s). **Middle, Bottom:** Longitudinal *in vivo* multiphoton images of the same layer II/III neurons before and after cytokine injection; from **left** to **right** respectively: baseline, 3 days, 10 days and 17 days post cytokine injection. **Middle**: Grayscale images of GCaMP6s channel masked and color-coded for cytoplasmic Ca^{2+} events per minute. **Bottom**: Representative Ca^{2+} activity traces displayed as delta f/f for the neurons marked in the left panel. (**b**) Cumulative plots of the neuronal activity for the entire population of neurons investigated at different timepoints after cytokine injection in healthy animals. **Inset**: Mean neuronal activity normalized to baseline for each time point shown as mean ± SEM (n=4 cytokine injected mice, tested with Shapiro-Wilk test and one-way ANOVA). (**c**) Heat map representation of the single neurons' activities before and after cytokine injection. Scale bar in **a**, 20μm.

Supplementary Figure 5 – Myelination recovers more slowly than neuronal activity.

(**a-c**) **Top**: Schematic of experimental design for longitudinal *in vivo* SCoRe imaging of myelin within the top 50 µm of layer I in the somatosensory cortex of sham injected mice (**a**), c-MS mice (**b**) and in cytokine injected non-immunized mice (**c**). (**a-c**) **Bottom**: Longitudinal *in vivo* SCoRe images of the same layer 1 area. From **left** to **right** respectively: (**a**) baseline, 3 days, 10 days and 17 days post sham injection. (**b**) MOG baseline, 3 days, 10 days and 17 days post cytokine injection. (**c**) baseline, 3 days, 10 days and 17 days post cytokines injection. (**d**) Percentage of SCoRe signal compared to baselines for sham and cytokine only injection and to baseline MOG for the c-MS model, 3 days, 10 days and 17 days post injection shown as mean ± SEM (n=3 for sham, cytokine only and c-MS mice, Shapiro-Wilk test and one-way ANOVA followed by Bonferroni's multiple comparisons test has been performed). (**e**) Electron micrographs of the cortical layer I of sham injected (**left**) and c-MS mice (**right**) showing myelin sheath (black arrowheads) 3 days post injection. (**f**) Myelin sheath density in layer I of somatosensory cortex in sham injected and c-MS mice at 3 days and 10 days post injection shown as mean ± SEM (tested in n=4 sham injected and n=4 c-MS mice for day 3 and n=5 sham injected and n=3 c-MS mice for day 10, Shapiro-Wilk test and one-way ANOVA followed by Bonferroni's multiple comparisons test). Scale bar in **a**, **b, c**, 20µm; **e**, 1µm. ***P<0.001, *P<0.05

Supplementary Figure 6 – Ratiometric imaging of calcium levels in the somata and dendrites of cortical neurons.

(**a**) *In vivo* multiphoton projection images of layer II/III neuronal somata and their Ca^{2+} levels in c-MS mice. Neurons were labelled using the viral vector AAV1.hSyn.mRuby2.Gcamp6s (see Methods), allowing for ratiometric measurements (GCamp6s/mRuby) of baseline neuronal Ca^{2+} concentration. Grayscale images of GCamp6s channel (**top**), ratiometric (GCamp6s/mRuby) images masked and color-coded for cytoplasmic Ca^{2+} (**bottom**). (**b**) *In vivo* multiphoton projection images of apical tuft dendrites and their Ca^{2+} levels in acute c-MS (d2/d3) mice, labelled with AAV1.hSyn1.Twitch2b. Grayscale images of YFP channel (**top**), ratiometric (YFP/CFP) images masked and color-coded for cytoplasmic Ca^{2+} (**bottom**). Example of a high Ca^{2+} dendrite exhibiting swellings (arrowheads). (**c**) Ca^{2+} concentration of single somata in control (sham injection, 'Ctr') and c-MS (d3) mice, plotted as GCamp6s/mRuby channel ratios normalized to control mean. 95% Confidence Interval 0.99-1.01 for control mean and 0,86-0.89 for c-MS mean.**Top:** Percentage of somata per animal with Ca^{2+} concentration > 3SD above control mean, shown as mean ± SEM (tested per animal in n=2 control and n=3 c-MS mice, Mann-Whitney U test). (**d**) Ca^{2+} concentration of single dendrites in healthy control ('Ctr') and c-MS d3 animals, plotted as YFP/CFP channel ratios normalized to control mean. 95% Confidence Interval 0.74-0.78 for control mean and 0.75-0.80 for c-MS mean. **Top:** Percentage of dendrites per animal with Ca^{2+} concentration >3SD above control mean, shown as mean ± SEM (tested per animal in n=8 control and n=17 c-MS mice, Mann-Whitney U test). Scale bars in **a, b**, 10 μm.

Supplementary Figure 7 – Temporal and spatial characteristics of monocyte infiltration and microglial activation in the c-MS model.

(**a, b**) Confocal projection images of cortex in healthy control (Ctr, **left**) and c-MS d3 (c-MS d3, **right**) *$CX_3CR\text{-}1^{GFP}$ x $Ccr2^{RFP}$* x *BiozziABH* mice. (**a**) Immunostaining for MHCII (red), as a marker of microglial activation, overlayed on the GFP signal of resident microglia (greyscale). (**b**) RFP signal of infiltrating phagocytes shown in red. (**c**) **Left:** Percentages of activated microglia (% MHCII positive/ all $CX_3CR\text{-}1^{GFP}$ cells) in healthy control (Ctr), only immunized (MOG), only cytokine injected (Cyto) and c-MS d3 mice. **Middle:** Time course of microglial activation (in %) 3 days, 7 days and 21 days after induction of cortical MS model (d3, d7, d21). **Right:** Distribution of microglial activation (in %) within the layers of the cortical column (Layer I, Layer II-IV and Layer V) and between injected (ipsilateral, 'ipsi') and non-injected hemisphere (contralateral, 'contra'). c-MS d3 data plotted in all 3 panels. Shown as mean ± SEM (tested per animal in n=2 control, n=2 MOG, n=3 Cyto, n=3 c-MS d3 mice; one-way ANOVA; Left: $F_{3,6}$=54.87, Middle $F_{2,6}$=441.6). (**d**) **Left:** Numbers of infiltrating phagocytes ($Ccr2^{RFP}$ cells) per standardized volume in healthy control (Ctr), only MOG immunized (MOG), only cytokine injected (Cyto) and c-MS d3 mice. **Middle:** Time course of phagocyte infiltration 3 days, 7 days and 21 days after induction of cortical MS model (d3, d7, d21). **Right:** Distribution of phagocyte infiltration within the layers of the cortical column (Layer I, Layer II-IV and Layer V) and between injected (ipsilateral) and non-injected hemisphere (contralateral). c-MS d3 data plotted in all 3 panels. Shown as mean ± SEM (tested per animal in n=2 naive, n=2 only MOG immunized, 'MOG', n=3 only cytokine injected, 'Cyto', n=3 c-MS d3 mice; one-way ANOVA; Left: $F_{3,6}$=24.47, Middle $F_{2,57}$=38.32). (**e**) Color-coded spatial matrix (11x8 squares) representing microglial activation (in %) of healthy control (Ctr, n=3, **left**) and c-MS d3 mice (n=3, **right**) mice ipsi- and contralateral to the cytokine injection site. (**f**) Color-coded matrix showing numbers of infiltrating phagocytes (Iba-1 positive, $CX_3CR\text{-}1^{GFP}$ negative cells) in healthy control (Ctr, n=3, **left**) and c-MS d3 mice (n=3, **right**) ipsi- and contralateral to injection site. Scale bar in **a** (applies also to **b**) 100 µm. ***P<0.001, **P<0.01, *P<0.05.

Supplementary Figure 8 – Treatment with CSF-1R inhibitor does not alter T cell infiltration into gray matter

(**a**) Image of CD4 immunostaining of c-MS d3 mice treated with vehicle (**left**, inset shows higher magnification, red arrowheads indicate CD4 positive cells). Quantification of the density of CD4 positive cells quantified ipsilateral and contralateral to the injected hemisphere in c-MS d3 mice treated with vehicle or CSF1-R inhibitor (**right**; n=5 mice per group; mean ± SEM; no significant difference was detected, unpaired t-test). (**b**) Image of CD8 immunostaining of c-MS d3 mice treated with vehicle (**left**, inset shows higher magnification, red arrowheads indicate CD8 positive cell). Quantification of the density of CD8 positive cells quantified ipsilateral and contralateral to the injected hemisphere in c-MS d3 mice treated with vehicle or CSF1-R inhibitor (**right**¸ n=5 mice per group; mean ± SEM; no significant difference was detected, unpaired t-test). Scale bar in **a** and **b** is 100 µm.

Supplementary Figure 9 – *In vitro* and *in vivo* effects of CSF1-R inhibitor treatment on CNS phagocytes

(**a**) Isolated primary murine microglia (untreated) show elevated MCP-1 (CCL2) after treatment with CSF-1. While adding DMSO does not change the levels of MCP-1, CSF1-R inhibitor treatment decreases the levels of MCP-1 in primary murine cells (n=3 in all groups, one-way ANOVA). (**b**) Isolated primary murine microglia (untreated) show elevated Il-12p40 after treatment with LPS. While adding DMSO does not change the levels of Il-12p40, CSF1-R inhibitor decreases the levels of Il-12p40 in primary murine cells (n=6 for untreated cells and n=5 for the other groups, one-way ANOVA). (**c-e**) FACS analysis of cell populations in brains of healthy controls (Ctr), MOG immunized and acute c-MS model mice treated with vehicle or CSF1-R inhibitor (n=3 mice were analyzed for healthy control and MOG immunized groups, n=10 mice were analyzed in c-MS model groups; mean ± SEM): (**c**) shows the proportion of $CD45^{int}$/ $CD11b^{int}$ cells (**left**) and their expression of CD40, MHCII and CD86 (**right**), (**d**) shows the proportion of $CD45^{high}$/ $CD11b^{high}$/ $Ccr2^{neg}$ cells (**left**) and their expression of CD40, MHCII and CD86 (**right**), (**e**) shows the proportion of $CD45^{high}$/ $CD11b^{high}$/ $Ccr2^{pos}$ cells (**left**) and their expression of CD40, MHCII and CD86 (**right**). (**f**) Different doses of CSF1-R inhibitor show no effect on the phagocytic activity of unstimulated primary mouse microglia, measured by uptake of pHrodo red-labeled synaptoneurosomes (n=4 wells per group). (**g**) CSF1 stimulation of primary mouse microglia leads to increased phagocytic activity. Treatment with 500 nM of CSF1-R inhibitor abrogated this effect (n=4 wells per group). One-way ANOVA followed by Tukey's multiple comparisons test was used in left panels, and two-way ANOVA in right panels of **c-e.** Two-way ANOVA in **f-g**. *** $P<0.001$, *$P<0.05$.

Supplementary Figure 10 – Confocal microscopy images illustrating the effect of CSF1-R inhibitor on CNS phagocytes

(**a**, **b**) Confocal projection images of cortex in a c-MS d3 *CX₃CR-1^{GFP} x BiozziABH* mouse treated with vehicle (**left**) or CSF1-R inhibitor (**right**). (**a**) GFP signal of resident microglia shown in greyscale. (**b**) Immunostaining for Iba-1 (red) overlayed on the GFP signal of resident microglia (greyscale). Yellow arrowheads indicate infiltrating Iba-1 positive, GFP negative phagocytes. (**c, e**) Xy/yz/xz-views of $CX_3CR\text{-}1^{GFP}$ or $Ccr2^{RFP}$cells (magenta) treated with vehicle (**left**) or CSF1-R inhibitor compound (**right**) showing Synapsin1(**up**) or Homer-1 (**down**) inclusions (cyan) colocalized with LAMP1 staining (white). (**c**) Xy/yz/xz-views of $CX_3CR\text{-}1^{GFP}$ cells (magenta) treated with vehicle (**left**) or CSF-1R inhibitor compound (**right**) showing Synapsin1 (**up)** or Homer-1 (**down**) inclusions (cyan) colocalized with LAMP1 staining (white). (**c**) Xy/yz/xz-views of $Ccr2^{RFP}$ cells (magenta) treated with vehicle (**left**) or CSF-1R inhibitor compound (**right**) showing Synapsin1 (**up)** or Homer-1 (**down**) inclusions (cyan) colocalized with LAMP1 staining (white). Scale bar in **a** and **b** 50 μm. Scale bar in **c** and **d** 10 μm.

Supplementary Figure 11 – Expression pattern of CSF1R and its ligands in human brain tissue

(**a**) t-Stochastic neighbor embedding (t-SNE) with subsequent cluster analysis of single-nucleus RNA-sequencing results (48,919 single nucleus profiles) from cortical gray matter and adjacent white matter of 12 progressive MS tissue blocks and 9 control tissue blocks published in Schirmer et al. . Distinct clusters are color-coded. (**b**) t-SNE plots with relative gene expression of CSF1R and its ligands CSF1 and interleukin 34 (IL34) highlighted in red. (**c**) t-SNE plots with relative gene expression of marker genes for identification of cell-specific clusters (as used in Schirmer et al.) highlighted in red. (**d**) Graphical representation of the expression of CSF1R, CSF1 and IL34 in selected cell clusters in MS and control samples. The diameter of each dot encodes the percentage of cells that express the respective gene within each cluster (the corresponding reference dots are shown in black on the bottom) and was calculated separately for cell clusters mapping to MS or control cases. The red color encodes the relative expression level of a given gene in all cells within the cluster.

Supplementary Figure 12 – Expression of immediate early genes in cMS mice treated with CSF1-R inhibitor

(**a**) c-Fos immunostaining in c-MS d3 mice treated with vehicle or CSF-1R inhibitor (inset shows higher magnification, red arrowheads indicate c-Fos positive cells). (**b**) Proportion of c-Fos positive cells among other haemalaun counterstained cells in layers II to IV in the ipsilateral or contralateral hemispheres of c-MS mice receiving vehicle or CSF1-R inhibitor (n=5 mice per group; mean ± SEM; no significant difference was detected, unpaired t-test). (**c**) c-Jun immunostaining in c-MS d3 mice treated with vehicle or CSF1-R inhibitor (inset shows higher magnification, red arrowheads indicate c-Jun positive cells). (**d**) Proportion of c-Jun positive cells among other haemalaun counterstained cells in layers II to IV in the ipsilateral or contralateral hemispheres of c-MS mice receiving vehicle or CSF1-R inhibitor (n=5 mice per group; mean ± SEM; no significant difference was detected, unpaired t-test.) Scale bar in **a** and **c** is 100 μm.

Caption for

Supplementary Movie 1 - Activity of single cortical neurons over the course of the cortical MS model.

Movie generated using FIJI software from 15 Hz recordings and displayed at 100 frames per second with a walking average of 3 (60 second recordings per time point).

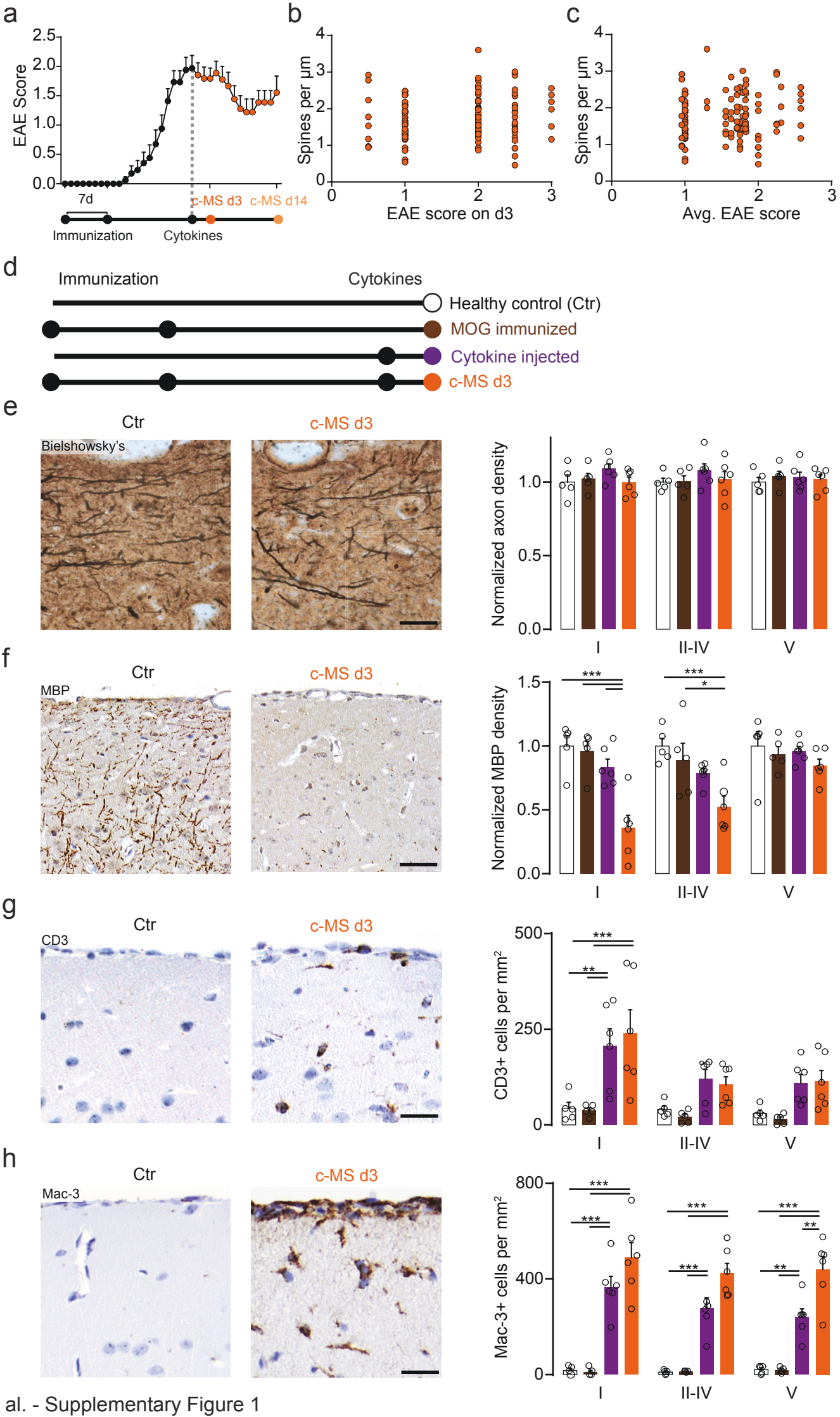

Jafari et al. - Supplementary Figure 1

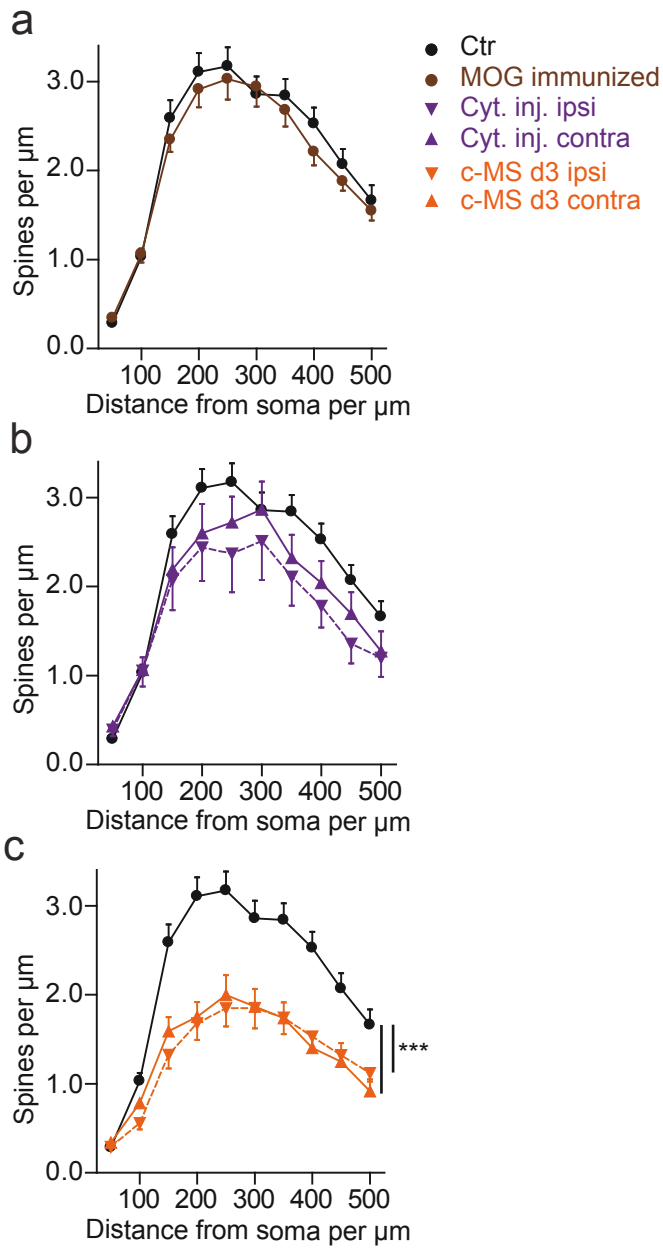
a
Ctr
MOG immunized
Cyt. inj. ipsi
Cyt. inj. contra
c-MS d3 ipsi
c-MS d3 contra
Spines per µm
3.0
2.0
1.0
0.0
100 200 300 400 500
Distance from soma per µm
b
Spines per µm
3.0
2.0
1.0
0.0
100 200 300 400 500
Distance from soma per µm
c
Spines per µm
3.0
2.0
1.0
0.0
***
100 200 300 400 500
Distance from soma per µm

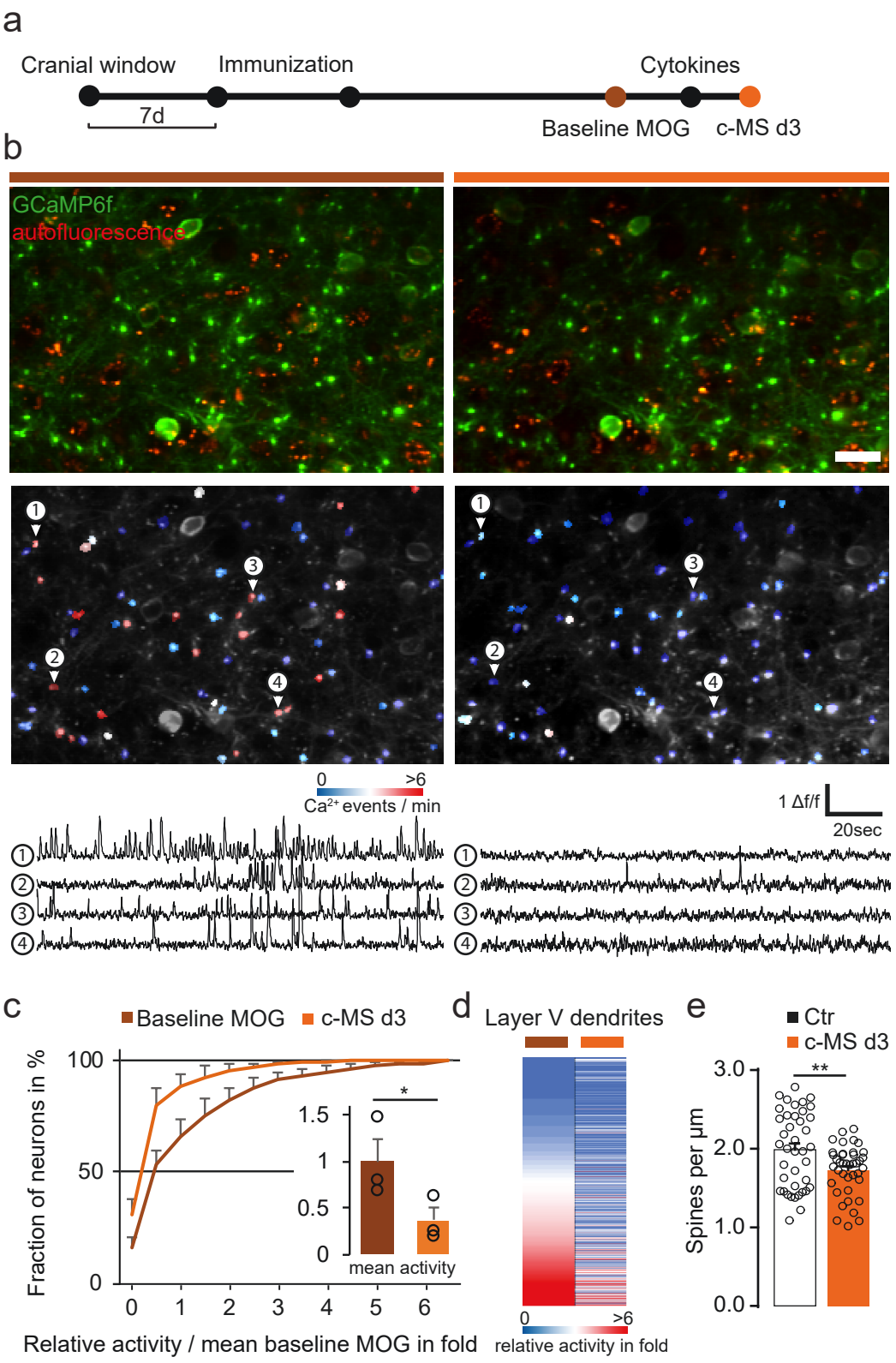
a
Cranial window
Immunization
Cytokines
7d
Baseline MOG
c-MS d3
b
GCaMP6f
autofluorescence
0
>6
Ca2+ events / min
1 Δf/f
20sec
c
Baseline MOG
c-MS d3
Fraction of neurons in %
100
50
0
0
1
2
3
4
5
6
1.5
1
0.5
0
*
mean activity
Relative activity / mean baseline MOG in fold
d
Layer V dendrites
0
>6
relative activity in fold
e
Ctr
c-MS d3
Spines per µm
3.0
2.0
1.0
0.0
**

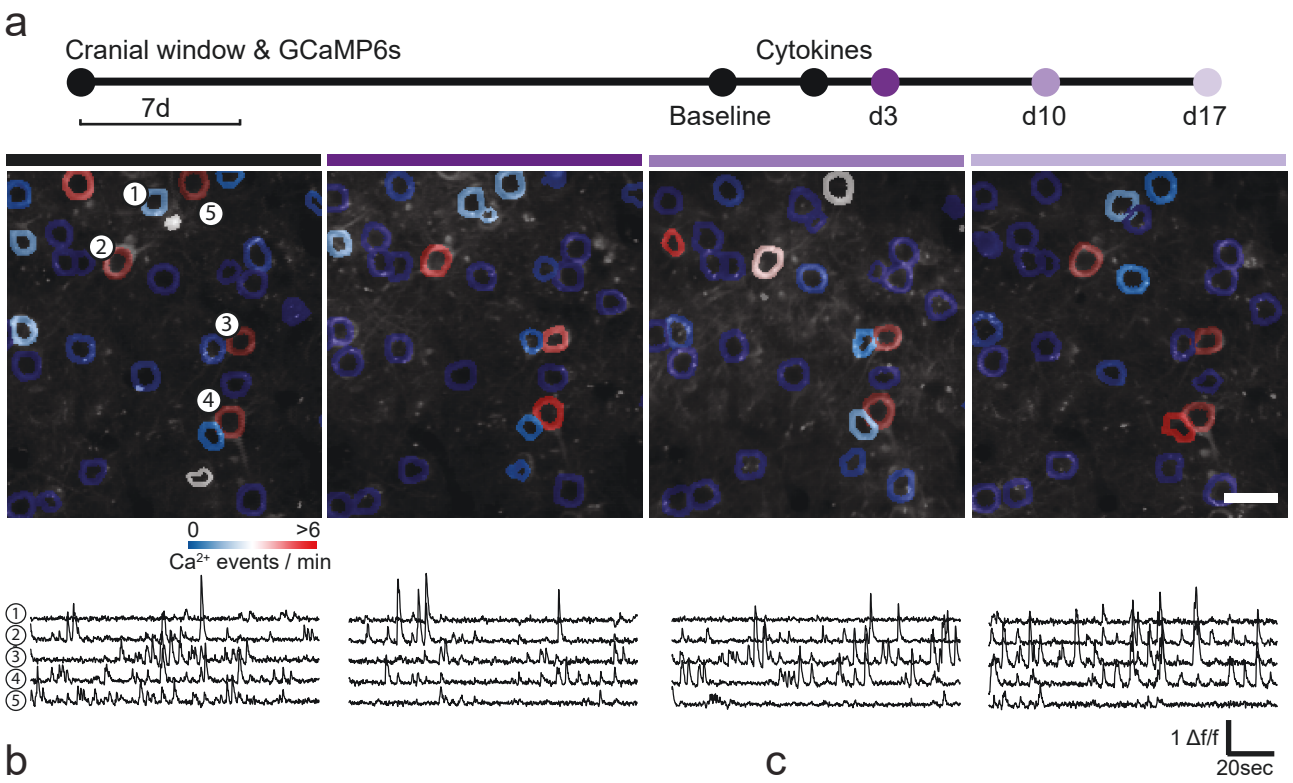
a
Cranial window & GCaMP6s
7d
Cytokines
Baseline
d3
d10
d17
0
>6
Ca2+ events / min
1 Δf/f
20sec

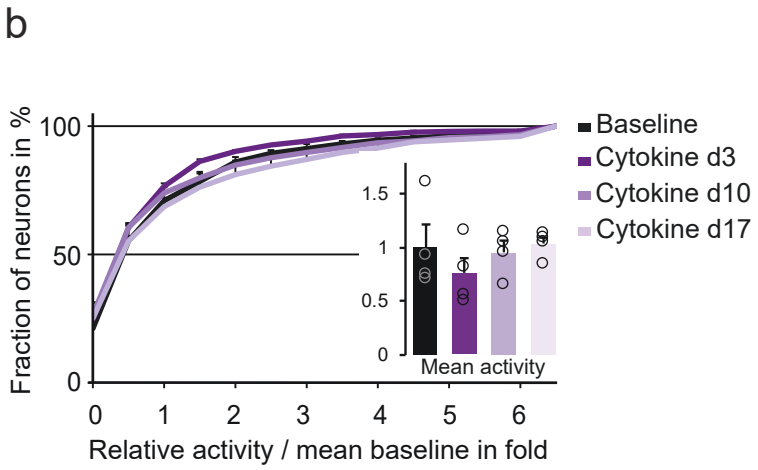
b
Fraction of neurons in %
100
50
0
0
1
2
3
4
5
6
Relative activity / mean baseline in fold
1.5
1
0.5
0
Mean activity
Baseline
Cytokine d3
Cytokine d10
Cytokine d17

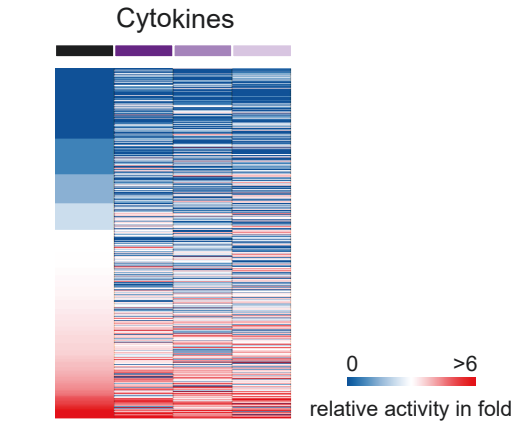
c
Cytokines
0
>6
relative activity in fold

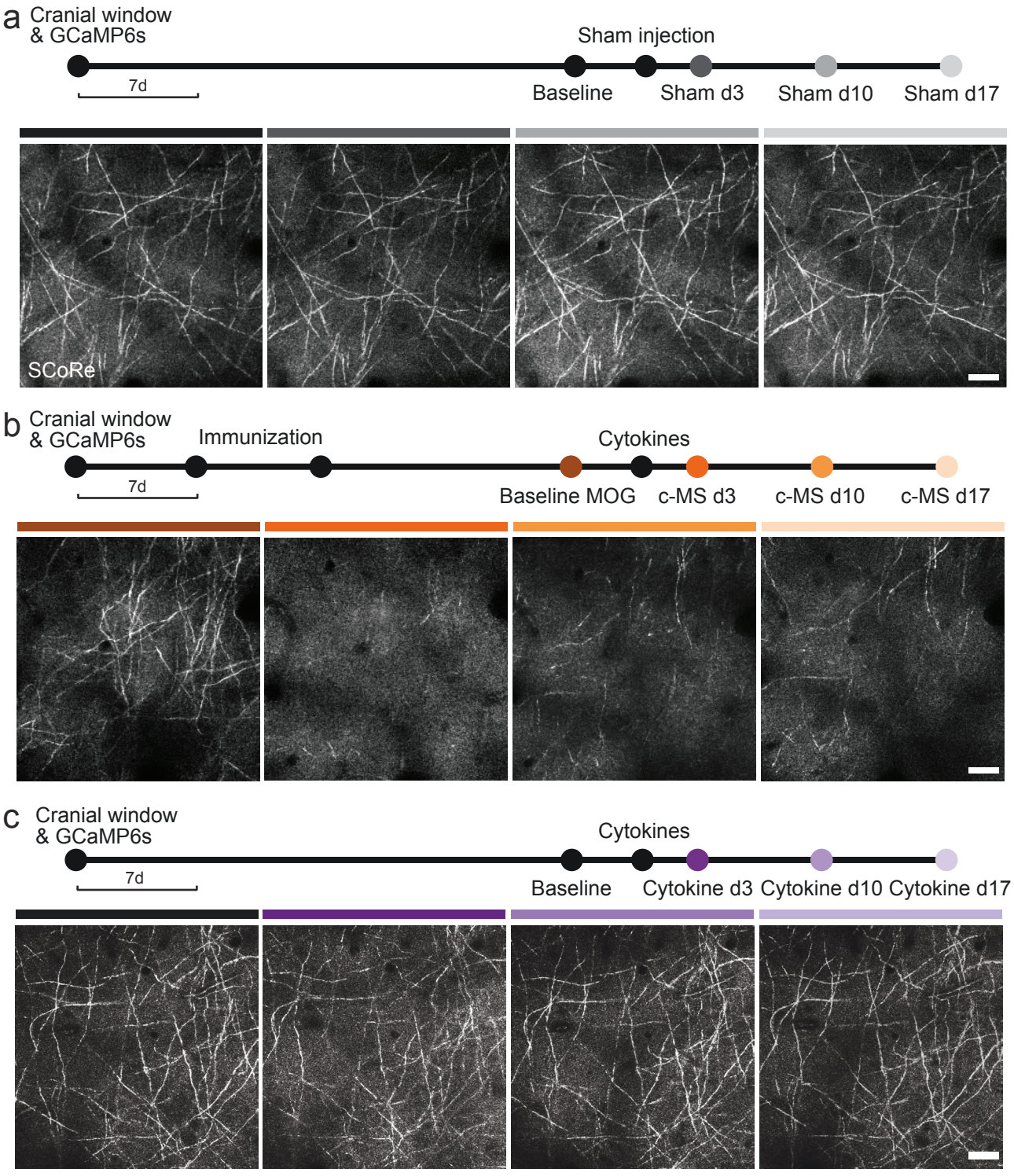
a
Cranial window
& GCaMP6s
7d
Sham injection
Baseline
Sham d3
Sham d10
Sham d17
SCoRe
b
Cranial window
& GCaMP6s
Immunization
7d
Cytokines
Baseline MOG
c-MS d3
c-MS d10
c-MS d17
c
Cranial window
& GCaMP6s
7d
Cytokines
Baseline
Cytokine d3
Cytokine d10
Cytokine d17
d
Sham
d3
d10
d17
c-MS
d3
d10
d17
Cytokine
d3
d10
d17
Myelin in % of baseline
100
50
0
***
e
f
Sham
d3
d10
c-MS
d3
d10
Myelin sheath per µm²
0.02
0.01
0.00
***
*

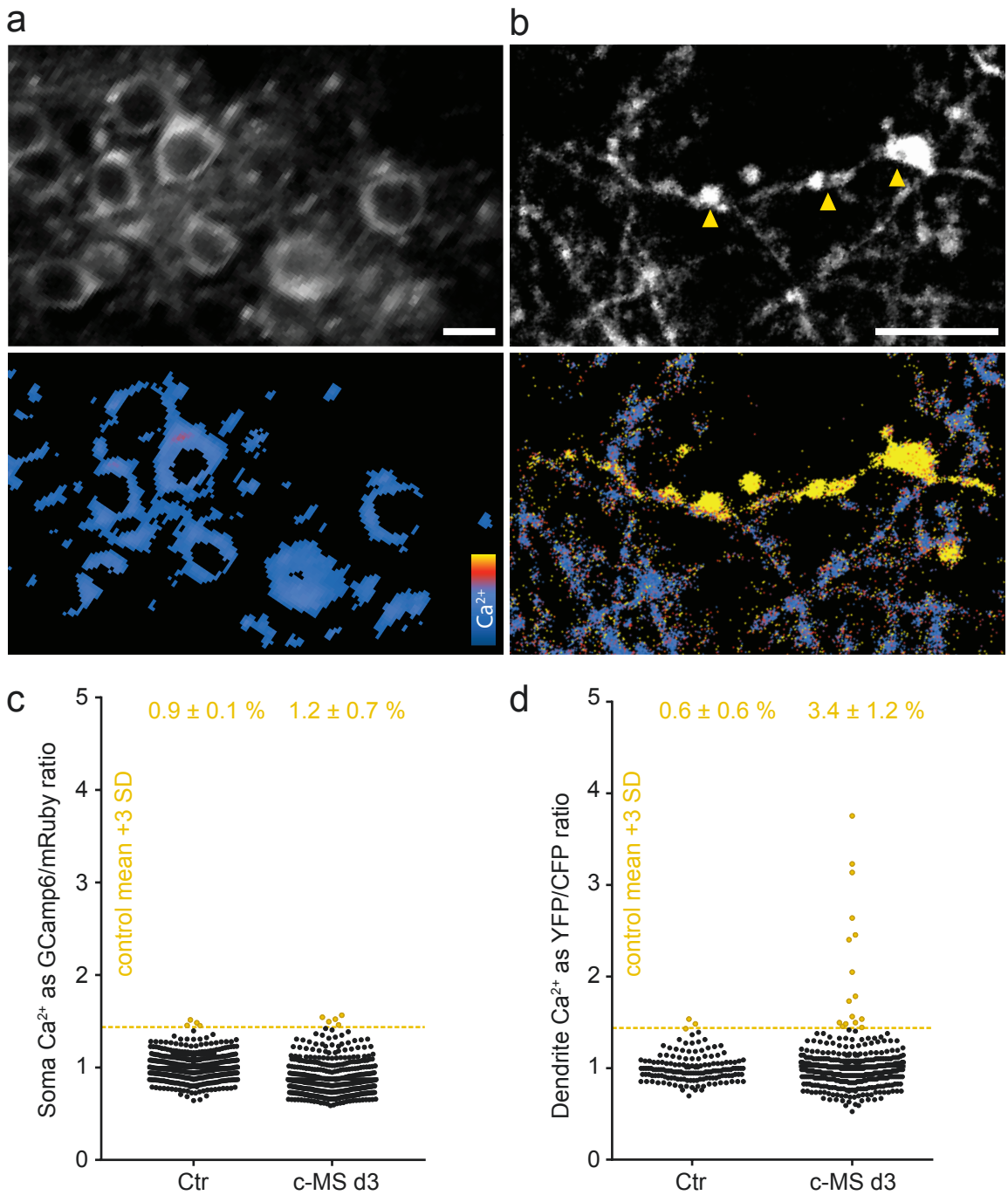
a
b
Ca2+
c
0.9 ± 0.1 %
1.2 ± 0.7 %
control mean +3 SD
Soma Ca2+ as GCamp6/mRuby ratio
0
1
2
3
4
5
Ctr
c-MS d3
d
0.6 ± 0.6 %
3.4 ± 1.2 %
control mean +3 SD
Dendrite Ca2+ as YFP/CFP ratio
0
1
2
3
4
5
Ctr
c-MS d3

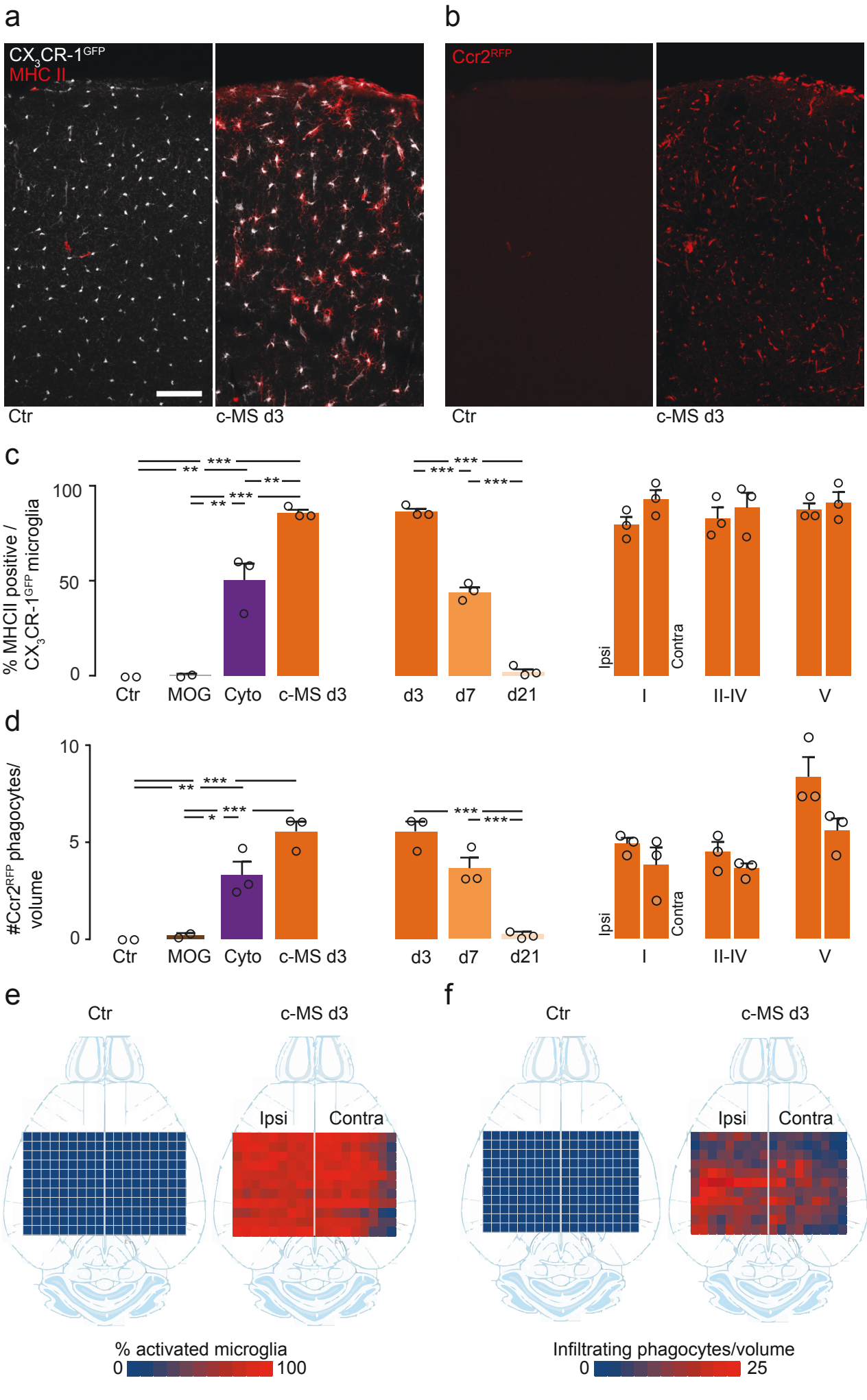

Jafari et al. - Supplementary Figure 7

a

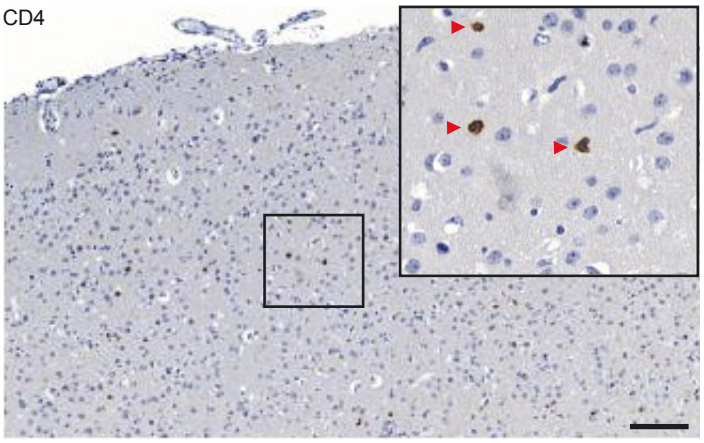
CD4

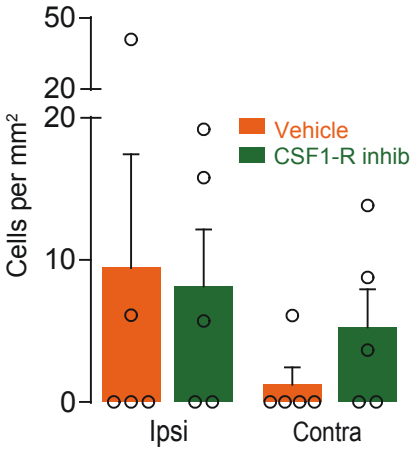
50
20
20
10
0
Cells per mm²
Vehicle
CSF1-R inhib
Ipsi
Contra

b

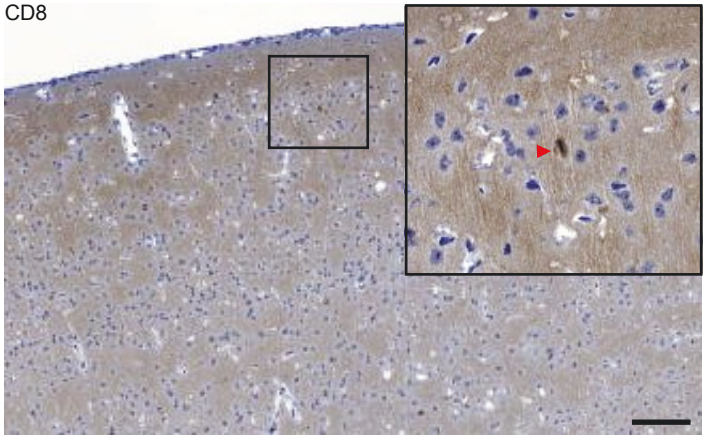
CD8

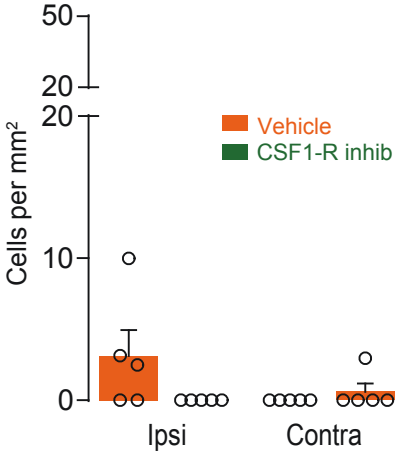
50
20
20
10
0
Cells per mm²
Vehicle
CSF1-R inhib
Ipsi
Contra

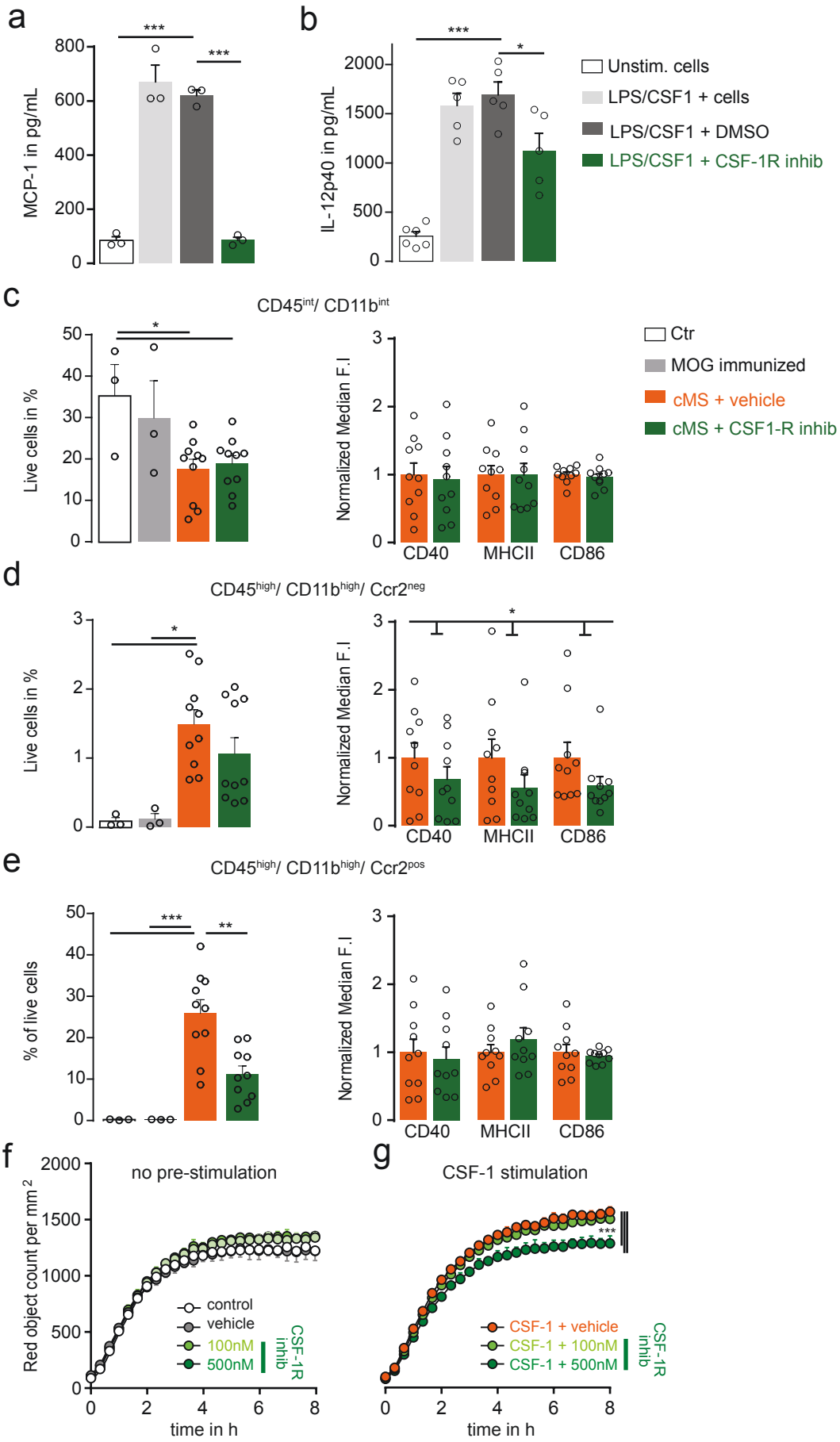
a
MCP-1 in pg/mL
b
IL-12p40 in pg/mL
Unstim. cells
LPS/CSF1 + cells
LPS/CSF1 + DMSO
LPS/CSF1 + CSF-1R inhib
c
CD45int/ CD11bint
Live cells in %
Normalized Median F.I
CD40
MHCII
CD86
Ctr
MOG immunized
cMS + vehicle
cMS + CSF1-R inhib
d
CD45high/ CD11bhigh/ Ccr2neg
e
CD45high/ CD11bhigh/ Ccr2pos
% of live cells
f
no pre-stimulation
Red object count per mm 2
time in h
control
vehicle
100nM
500nM
CSF-1R inhib
g
CSF-1 stimulation
CSF-1 + vehicle
CSF-1 + 100nM
CSF-1 + 500nM

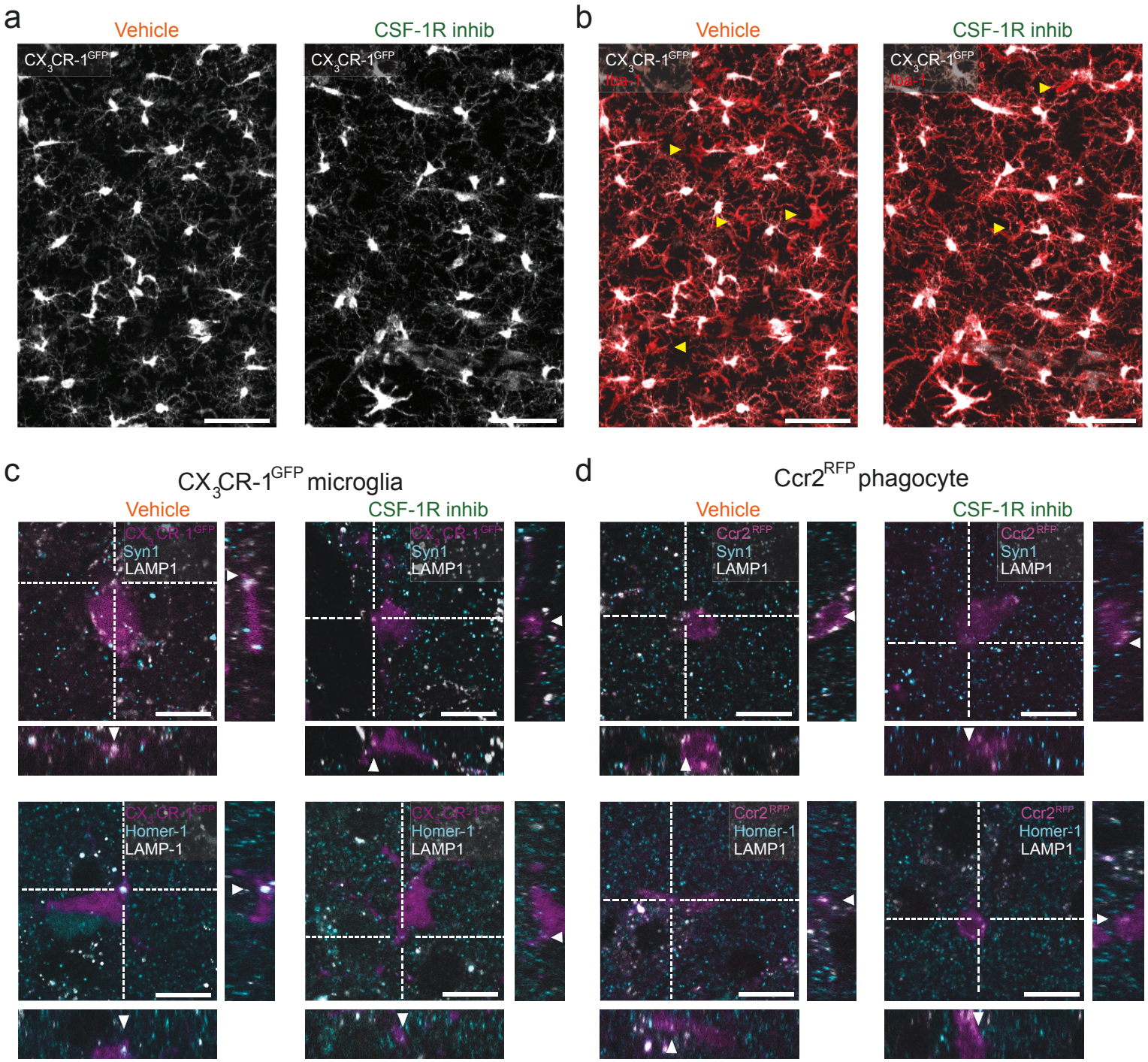
a
Vehicle
CSF-1R inhib
CX3CR-1GFP
b
Vehicle
CSF-1R inhib
CX3CR-1GFP
Iba-1
c
CX3CR-1GFP microglia
Vehicle
CSF-1R inhib
CX3CR-1GFP
Syn1
LAMP1
Homer-1
LAMP-1
d
Ccr2RFP phagocyte
Vehicle
CSF-1R inhib
Ccr2RFP
Syn1
LAMP1
Homer-1

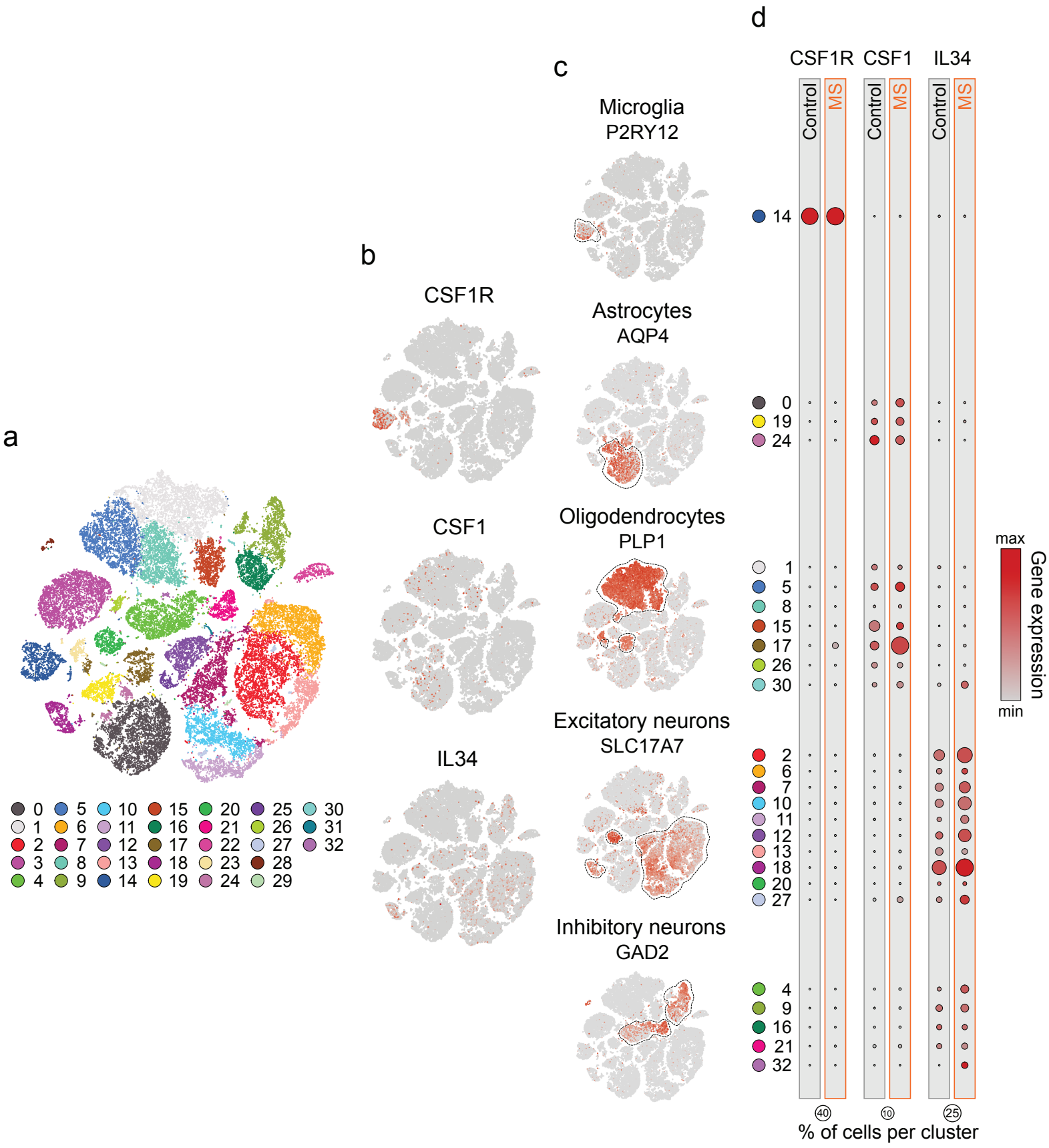
a
0 5 10 15 20 25 30
1 6 11 16 21 26 31
2 7 12 17 22 27 32
3 8 13 18 23 28
4 9 14 19 24 29
b
CSF1R
CSF1
IL34
c
Microglia
P2RY12
Astrocytes
AQP4
Oligodendrocytes
PLP1
Excitatory neurons
SLC17A7
Inhibitory neurons
GAD2
d
CSF1R
CSF1
IL34
Control
MS
14
0
19
24
1
5
8
15
17
26
30
2
6
7
10
11
12
13
18
20
27
4
9
16
21
32
40
10
25
% of cells per cluster
max
min
Gene expression

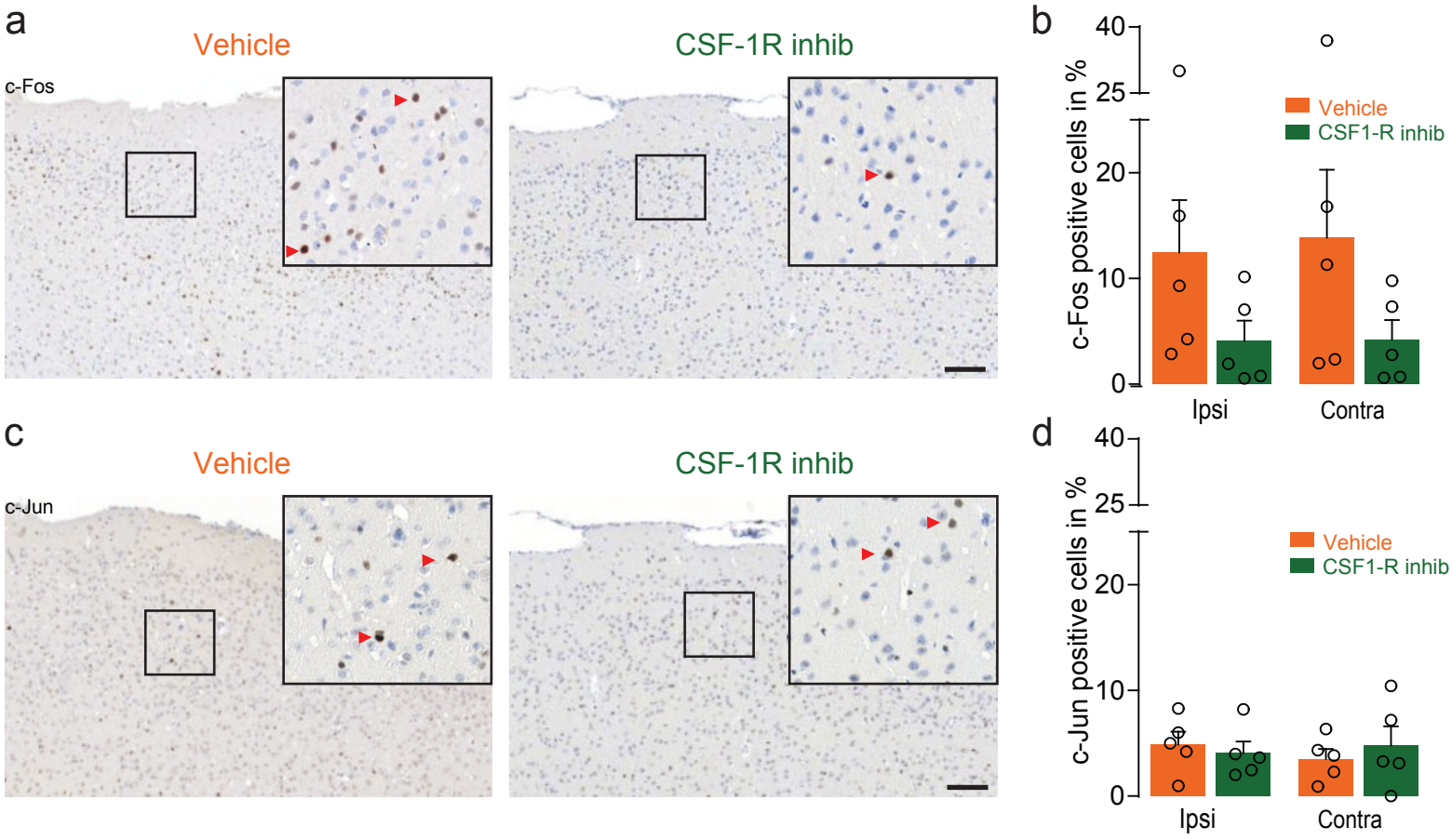
a
Vehicle
CSF-1R inhib
c-Fos
b
c-Fos positive cells in %
40
25
20
10
0
Vehicle
CSF1-R inhib
Ipsi
Contra
c
Vehicle
CSF-1R inhib
c-Jun
d
c-Jun positive cells in %
40
25
20
10
0
Vehicle
CSF1-R inhib
Ipsi
Contra